Rayleigh-enhanced attosecond sum-frequency polarization beats via twin color-locking noisy lights

Yanpeng Zhang,[1,*] Chenli Gan,[2] Long Li,[1] Ruiqiong Ma,[1] Jianping Song,[1] Tong Jiang,[1] Xiaojun Yu,[1] Chuangshe Li,[1] Hao Ge,[1] and Keqing Lu[3]

[1]*Department of Electronic Science and Technology, Xi'an Jiaotong University, Xi'an 710049, China*

[2]*Department of Physics, P. O. Box 311427, University of North Texas, Denton, Texas 76203-1427, USA*

[3]*State Key Laboratory of Transient Optics and Technology, Xi'an Institute of Optics and Precision Mechanics, Chinese Academy of Sciences, Xi'an 710068, China*

(Received 22 February 2005; published 18 July 2005)

Based on color-locking noisy field correlation, a time-delayed method is proposed to suppress the thermal effect, and the ultrafast longitudinal relaxation time can be measured even in an absorbing medium. One interesting feature in field-correlation effects is that Rayleigh-enhanced four-wave mixing (RFWM) with color-locking noisy light exhibits spectral symmetry and temporal asymmetry with no coherence spike at $\tau=0$. Due to the interference between the Rayleigh-resonant signal and the nonresonant background, RFWM exhibits hybrid radiation-matter detuning with terahertz damping oscillations. The subtle Markovian high-order correlation effects have been investigated in the homodyne- or heterodyne-detected Rayleigh-enhanced attosecond sum-frequency polarization beats (RASPBs). Analytic closed forms of fourth-order Markovian stochastic correlations are characterized for homodyne (quadratic) and heterodyne (linear) detection, respectively. Based on the polarization interference between two four-wave mixing processes, the phase-sensitive detection of RASPBs has also been used to obtain the real and imaginary parts of the Rayleigh resonance.

DOI: 10.1103/PhysRevA.72.013812 PACS number(s): 42.65.Es, 42.65.Re, 42.50.Ar, 42.65.Hw

I. INTRODUCTION

Polarization beats between two excitation pathways are related to recent studies on quantum interference [1–3]. They can be observed even without using stabilized tunable lasers. Phenomena such as electromagnetically induced transparency (EIT), enhanced index of refraction, and lasing without population inversion have been predicated theoretically and demonstrated experimentally [4,5]. The interest in these phenomena is due, on one hand, to the fundamental nature of atomic coherence effects and, on the other hand, to possible applications. Specifically, some interesting linear and nonlinear optical properties of three-level EIT systems have been described [4,5], such as absorption reduction, sharp dispersion change, and enhanced Kerr nonlinearity. The linear absorption reduction on resonance is due to atomic coherence established between states and by the two laser beams, or can be considered as destructive interference between the two channel transition probabilities (two competing processes), as easily seen in the dressed-state picture. Our work is also closely related to Raman quantum beats [3] or coherent Raman spectroscopy (CRS). CRS is a powerful tool for studying the vibrational or rotational modes of a molecule. The most widely used CRS techniques include stimulated Raman gain spectroscopy, coherent anti-Stokes Raman scattering (CARS), and Raman-induced Kerr-effect spectroscopy. CARS is one type of two-color nonlinear laser spectroscopy. In CARS, the beat between two beams at frequencies ω_1 and ω_2 will coherently excite Raman-active modes in the media if $\omega_1-\omega_2$ equals the Raman resonant frequency. The material excitational wave is then mixed with the beam at ω_1 to yield a coherent output at the anti-Stokes frequency $\omega_s=2\omega_1-\omega_2$. Compared with conventional Raman scattering, CARS is much less sensitive to sample fluorescence and has the capability of high spectral resolution. However, strict phase matching is required.

Phase-locking ultrashort-pulse nonlinear optical spectroscopy has proved to be a valuable technique for investigating the dynamics of a wealth of mechanisms in condensed matters. Using femtosecond time-resolved four-wave mixing (FWM), valuable information on the dephasing dynamics in semiconductors and molecular materials has been obtained. The time resolution of this method is limited by the pulse width. The ultrafast dephasing phenomena can also be studied by time-delayed FWM with incoherent light [6,7]. This technique is intrinsically related to optical coherent transient spectroscopy, with the advantage that the time resolution is determined by the correlation time τ_c of the color-locking noisy light source. Rayleigh-type FWM is a nonresonant process and a frequency-domain nonlinear laser spectroscopy with high frequency resolution, which is determined by the laser linewidth. Since the relaxation time is deduced from the FWM spectrum, the measurement is not limited by the laser pulse width or the laser correlation time [6,7].

Lasers are inherently noisy devices, in which both the phase and amplitude of the field can fluctuate. Noisy light can be used to probe atomic and molecular dynamics, and it offers a unique alternative to the more conventional frequency-domain spectroscopies and ultrashort-pulse time-domain spectroscopies. Color-locking noisy light is an intermediate between cw and short-pulse methods [8–16]. Color locking results in complete cancellation of the spectrally broad noise carried by the noisy light [8]. DeBeer *et al.* [1] first performed a 980-as sum-frequency ultrafast modulation spectroscopy (UMS) experiment. Bogdanov *et al.* have also

*Corresponding author. Electronic address: ypzhang@mail.xjtu.edu.cn

showed attosecond beats with different sources: interference of the Rayleigh scattering field and the FWM field of phase-locking ultrashort laser pulses [2]. Rayleigh-enhanced attosecond sum-frequency polarization beating (RASPB) is one interesting way to study the stochastic properties of light [17,18]. Previous extensive noisy-light-based CRS, either CARS or coherent Stokes Raman scattering (CSRS) yield both Raman frequencies via radiation difference oscillations and dephasing times in the interferometric time domain. Unlike in RASPB in those spectroscopies the presence of one monochromatic beam is essential [8–16]. The characteristics of the interferogram of RASPB are a result of two main components: the material response (resonant term) and the light response (nonresonant term) along with the interplay between the two responses.

This paper addresses the role of noise in the incident fields on the nature of the wave-mixing signal in the time and frequency domains. This important topic has been already treated extensively in the literature [19]. Ulness *et al.* invented the factorized time correlator diagram "synchronization" and "accumulation" analysis for noisy light response [8–16], instead of double-sided Feynman diagrams. A fundamental principle of noisy light spectroscopy is color locking which results as a consequence of the phase-incoherent nature of the light. Color locking is responsible for the complete and utter cancellation of the noise spectrum carried by the noisy light used to produce it [8]. On the other hand, there should be two classes of such component beams. In one class the components are derived from separate lasers and their mixed (cross) correlators should vanish. In the second case the two components are derived from a single laser source whose spectral output is doubly peaked. This can be created from a single dye laser in which two different dyes in solution together are amplified [13–16]. The present paper deals only with the first class. That is to say, we are considering only the class of two-color beams in which each color is derived from a separate noisy light source. The double-peaked beams 1 and 2 [Figs. 1(a) and 1(b)] are paired and correlated, but each of the peaks is uncorrelated. Beam 3, having one of the peaks (from another noisy light source) found in twin beams 1 and 2, is dependent on and correlated with twin beams 1 and 2. In any case the literature has already explored both theoretically and experimentally the use of such multicolor noisy light in FWM [8–16]. Interestingly, that work only treats the second class of multicolored beams (a single laser source for the multipeaked "tailored" light) in difference-frequency self-diffraction geometry. Also that work did not treat the RASPB with sum-frequency phase-conjugation geometry using three types of noisy models and furthermore its beam 3 was not noisy (it was "monochromatic"). In this paper, based on the field correlation of color-locking twin noisy lights, the homodyne-detected RFWM and RASPB, heterodyne- and detected RASPB have been investigated, respectively. An analytic closed form of the results is obtained.

II. BASIC THEORY

The RASPB is a third-order nonlinear polarization beat phenomenon. The polarization beat is based on interference at the detector between FWM signals which originate from macroscopic polarizations excited simultaneously in a homogeneous [17,18] or inhomogeneous [20–26] broadened sample. It critically requires that all the polarizations have the same frequency. The basic geometry is shown in Fig. 1(a). The twin beams 1 and 2 consist of two central circular frequency components ω_1 and ω_2; a small angle exists between them. Beam 3 with central circular frequency ω_3 is almost propagating along the opposite direction to beam 1. In an optical Kerr medium (no thermal grating effects), the nonlinear interaction of beams 1 and 2 with the medium gives rise to two molecular-reorientational gratings, i.e., ω_1 and ω_2 will induce their own nonresonant static gratings G1 and G2, respectively. Two FWM signals are the results of the diffraction of beam 3 by G1 and G2, respectively. Now, if the frequency detuning $\Delta=\omega_3-\omega_1$ is much smaller than $\Delta'=\omega_3-\omega_2$ (i.e., $\Delta\ll\Delta'$ and $\Delta\approx 0$) (Fig. 1), a large-angle resonant moving grating formed by the interference between the ω_1 frequency component of beam 2 and the ω_3 frequency component of beam 3, will excite the Rayleigh mode of the medium and enhance the FWM signal of G1 (i.e., RFWM). Finally, polarization beats originate from the interference between the macroscopic polarizations from the RFWM process and the nondegenerate FWM (NDFWM) process. The beat signal (beam 4) is along the opposite direction of beam 2 approximately.

In a typical experiment, the ω_1 and ω_2 two-color light sources enter a dispersion-compensated Michelson interferometer to generate identical twin composite beams. Twin composite stochastic fields of beam 1, $E_{p1}(\mathbf{r},t)$, and beam 2, $E_{p2}(\mathbf{r},t)$ for a homodyne detection scheme of attosecond sum-frequency RASPB, can be written as

$$\begin{aligned} E_{p1} &= E_1(\mathbf{r},t) + E_2'(\mathbf{r},t) \\ &= \varepsilon_1 u_1(t)\exp[i(\mathbf{k}_1\cdot\mathbf{r}-\omega_1 t)] \\ &\quad + \varepsilon_2' u_2(t-\tau)\exp[i(\mathbf{k}_2'\cdot\mathbf{r}-\omega_2 t+\omega_2\tau)], \end{aligned} \tag{1}$$

$$\begin{aligned} E_{p2} &= E_1'(\mathbf{r},t) + E_2(\mathbf{r},t) \\ &= \varepsilon_1' u_1(t-\tau)\exp[i(\mathbf{k}_1'\cdot\mathbf{r}-\omega_1 t+\omega_1\tau)] \\ &\quad + \varepsilon_2 u_2(t)\exp[i(\mathbf{k}_2\cdot\mathbf{r}-\omega_2 t)]. \end{aligned} \tag{2}$$

Here, $\varepsilon_i,\mathbf{k}_i$ ($\varepsilon_i',\mathbf{k}_i'$) are the constant field amplitude and the wave vector of the ω_i component in beam 1 (beam 2), respectively. $u_i(t)$ is a dimensionless statistical factor that contains phase and amplitude fluctuations. The $u_i(t)$ is taken to be a complex ergodic stochastic function of t, which obeys complex circular Gaussian statistics in a chaotic field. τ is a variable relative time delay between the prompt (unprimed) and delayed (primed) fields. To accomplish this the frequency components ω_1 and ω_2 are split and recombined to provide two double-frequency pulses in such a way that the ω_1 component is delayed by τ in beam 2 and the ω_2 component delayed by the same amount in beam 1 [Figs. 1(a) and 1(c)]. A time delay τ is introduced in both composite beams, which is quite different from Rayleigh-enhanced femtosecond difference-frequency polarization beats (RFDPB) [Figs.

(a)

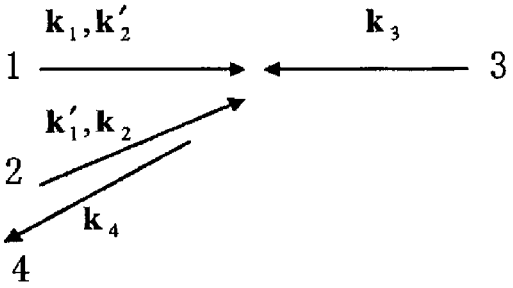

(b)

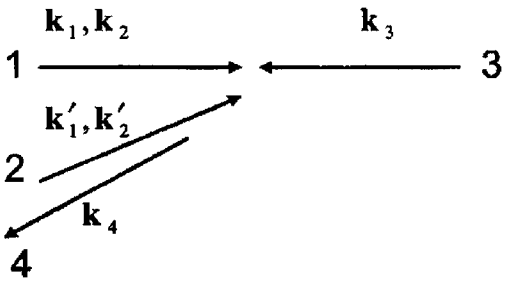

(c)

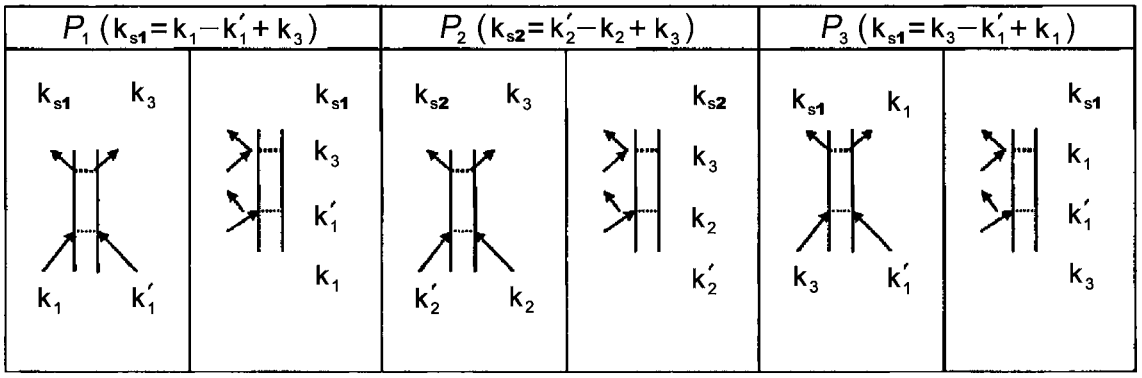

(d)

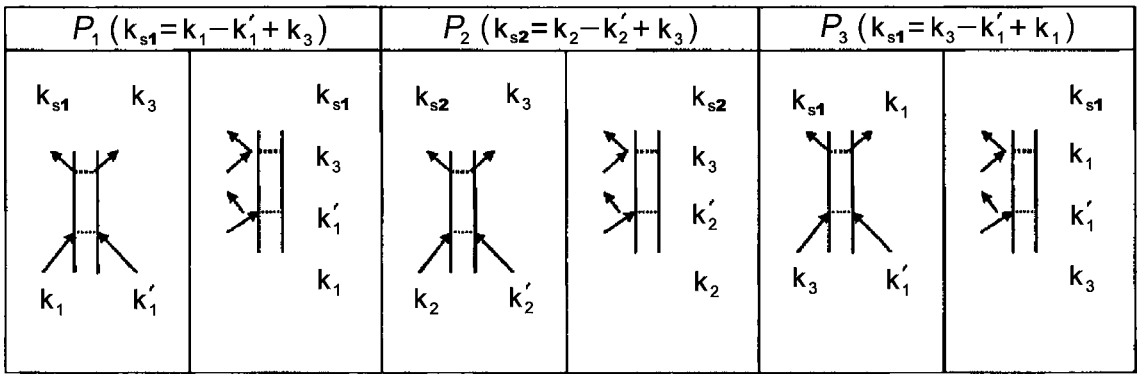

FIG. 1. Phase-conjugation geometry of RASPB for (a) and RFDPB for (b), respectively; double-sided Feynman diagrams representing the Liouville pathways for P_1, P_3, and P_2 for RASPB (c) and RFDPB (d), respectively.

1(b) and 1(d)] [17,18]. On the other hand, the complex electric fields of beam 3 can be written as

$$E_3(\mathbf{r},t) = \varepsilon_3 u_3(t)\exp[i(\mathbf{k}_3 \cdot \mathbf{r} - \omega_3 t)]. \tag{3}$$

Here, ω_3, ε_3, and $\mathbf{k}_3$ are the frequency, the field amplitude, and the wave vector of the field, respectively.

The order parameters Q_1 and Q_2 of two nonresonant static gratings induced by beams 1 and 2 satisfy the following equations [17,18]:

$$\frac{dQ_1}{dt} + \gamma Q_1 = \chi\gamma E_1(\mathbf{r},t)[E_1'(\mathbf{r},t)]^*, \tag{4}$$

$$\frac{dQ_2}{dt} + \gamma Q_2 = \chi\gamma E_2'(\mathbf{r},t)[E_2(\mathbf{r},t)]^*. \tag{5}$$

Here γ and χ are the relaxation rate and the nonlinear susceptibility of the two static gratings, respectively. The optical Kerr effect for the liquid CS_2 has at least two components, i.e., a relatively long "Debye" component and a shorter "interaction-induced" component.

We consider a large-angle resonant moving grating formed by the interference of beams 2 and 3, and the order parameter Q_3 satisfies the following equation:

$$\frac{dQ_3}{dt} + \gamma Q_3 = \chi\gamma[E_1'(\mathbf{r},t)]^* E_3(\mathbf{r},t). \tag{6}$$

The induced three third-order nonlinear polarizations which are responsible for the FWM signals are

$$\begin{aligned} P_1 &= Q_1(\mathbf{r},t)E_3(\mathbf{r},t) \\ &= S_1(\mathbf{r})\int_0^\infty u_1(t-t')u_1^*(t-t'-\tau)u_3(t)\exp(-\gamma t')dt', \end{aligned} \tag{7}$$

$$\begin{aligned} P_2 &= Q_2(\mathbf{r},t)E_3(\mathbf{r},t) \\ &= S_2(\mathbf{r})\int_0^\infty u_2^*(t-t')u_2(t-t'-\tau)u_3(t)\exp(-\gamma t')dt', \end{aligned} \tag{8}$$

$$\begin{aligned} P_3 &= Q_3(\mathbf{r},t)E_1(\mathbf{r},t) \\ &= S_1(\mathbf{r})\int_0^\infty u_1^*(t-t'-\tau)u_3(t-t')u_1(t)\exp[-(\gamma - i\Delta)t']dt', \end{aligned} \tag{9}$$

Here $S_1(\mathbf{r}) = \chi\gamma\varepsilon_1(\varepsilon_1')^*\varepsilon_3 \exp\{i[(\mathbf{k}_1 - \mathbf{k}_1' + \mathbf{k}_3)\cdot\mathbf{r} - \omega_3 t - \omega_1\tau]\}$, and $S_2(\mathbf{r}) = \chi\gamma\varepsilon_2'(\varepsilon_2)^*\varepsilon_3 \exp\{i[(\mathbf{k}_2' - \mathbf{k}_2 + \mathbf{k}_3)\cdot\mathbf{r} - \omega_3 t + \omega_2\tau]\}$.

In general, there are 48 terms in the third-order density operator for a FWM process. The number of Feynman diagrams at jth order (for cw experiments) corresponds to the number of Liouville pathways 2^j multiplied by the number of distinct temporal field orderings (as many as $j!$) for the given process. Therefore, at third order, where beams 1, 2, and 3 are distinct, there are $2^j j! = 48 (j=3)$ different Feynman diagrams at the polarization level. Often the experimental constraints reduce the number of diagrams to a significantly smaller subset which dominate the behavior of the signal. We are strictly in the full (or partial) rotating-wave approximation and omit most of the $2^j j!$ Liouville pathways formally present in three-color FWM. More specifically, phase-matching and frequency selection of the FWM signals along $\mathbf{k}_4$ greatly restrict the third-order perturbative pathways (Fig. 1). Moreover, polarization beating is based on the interference at the detector between FWM signals, which originate from the macroscopic polarizations excited simultaneously in the sample. It is preferred that all the polarizations have the same frequency. The frequencies of P_1, P_2, and P_3 are ω_3, while P_{R2} and P_{R3} have frequencies $\omega_1 - \omega_2 + \omega_3$ and $\omega_2 - \omega_1 + \omega_3$, respectively [17,18]. Furthermore, due to the phase mismatching, the FWM signals from P_{R2} and P_{R3} are usually much smaller than those from P_1, P_2, and P_3. So the third-order nonlinear polarizations P_1, P_3 (with Lorentzian line shape for Rayleigh mode), and P_2 have the same frequency ω_3, $P_1 + P_3$ and P_2 correspond to the RFWM and NDFWM processes which have wave vectors $\mathbf{k}_1 - \mathbf{k}_1' + \mathbf{k}_3$ and $\mathbf{k}_2' - \mathbf{k}_2 + \mathbf{k}_3$, respectively [Figs. 1(a) and 1(c)].

III. STOCHASTIC CORRELATION EFFECTS OF RFWM

We have the total third-order polarization $P^{(3)} = P_1 + P_3$ for the RFWM. For the macroscopic system where phase matching takes place this signal must be drawn from the $P^{(3)}$ developed on one "atom" multiplied by the $(P^{(3)})^*$ that is developed on another "atom" which must be located elsewhere in space (with summation over all such pairs). For homodyne detection the RFWM signal is proportional to the average of the absolute square of $P^{(3)}$ over the random variable of the stochastic process $\langle |P^{(3)}|^2 \rangle$, which involves fourth- and second-order coherence functions of $u_i(t)$. Although the bichromophoric model is needed to fully appreciate the subtle features of RFWM spectroscopy (especially the effects of the different Markovian noise models), it is interesting to first consider the approximation in which the averaging is done at the polarization level rather than the intensity level. This reduces the problem to only second-order field-correlation functions and in fact eliminates the differences in the three Markovian models considered here. This allows one greater insight into the importance of the higher-order field-correlation functions with respect to each of the Markovian models.

A. Kerr medium with a single relaxation rate of molecular-reorientational grating

The field-correlation effects in a medium which has a single relaxation rate γ have been considered in a Markovian noisy field. In the limit of $\gamma \gg \alpha_1, \alpha_3$ for the chaotic field model (CFM), we have $I(\Delta,\tau) \propto [1 + \exp(-2\alpha_1|\tau|)][1 + 3\gamma^2/(\gamma^2 + \Delta^2)]$ for both $\tau > 0$ and $\tau < 0$, the RFWM spectrum is independent of τ. Moreover, if we define a parameter $R = I_{\text{res}}(\Delta = 0)/I_{\text{nonres}}$ as the ratio between the resonant signal at $\Delta = 0$ and the nonresonant background, we have $R \approx 3$. We then consider the RFWM spectra in the limit of $\gamma \ll \alpha_1, \alpha_3$ for the CFM. We have

$$I(\Delta,\tau) \propto \frac{\gamma}{2\alpha_1} + \frac{\gamma(\alpha_1+\alpha_3)}{(\alpha_1+\alpha_3)^2+\Delta^2} + \left(1+\frac{2\gamma(\alpha_1+\alpha_3)}{(\alpha_1+\alpha_3)^2+\Delta^2}\right) \times \exp(-2\alpha_1|\tau|)$$

for $\tau>0$ and

$$I(\Delta,\tau) \propto \frac{\gamma}{2\alpha_1} + \frac{\gamma(\alpha_1+\alpha_3)}{(\alpha_1+\alpha_3)^2+\Delta^2} + \left(1+\frac{2\gamma(\alpha_1-\alpha_3)}{(\alpha_1-\alpha_3)^2+\Delta^2}\right)\exp(-2\alpha_1|\tau|) + \frac{4\gamma\alpha_1\exp[-(\alpha_1+\alpha_3)|\tau|]}{{\alpha_1}^4-2{\alpha_1}^2({\alpha_3}^2-\Delta^2)+({\alpha_3}^2+\Delta^2)^2} \times[({\alpha_1}^2-{\alpha_3}^2+\Delta^2)\cos(\Delta|\tau|)+2\alpha_3\Delta\sin(\Delta|\tau|)]$$

for $\tau<0$. The equation for $\tau>0$ indicates that when $\tau=0$ the nonresonant background is larger than the resonant signal by a factor of $(\alpha_1+\alpha_3)/3\gamma \gg 1$ at $\Delta=0$. However, when $\alpha_i|\tau| \gg 1$ then the resonant signal and the nonresonant background become comparable, and we have $R=2\alpha_1/(\alpha_1+\alpha_3)$, which equals 1 if $\alpha_1=\alpha_3$.

Secondly, we have considered the field-correlation effects in a single-relaxation-rate medium for the phase-diffusion model (PDM). In the limit of $\gamma \gg \alpha_1, \alpha_3$ [Fig. 2(a)], we have $I(\Delta) \propto 1+3\gamma^2/(\gamma^2+\Delta^2)$ for both $\tau>0$ and $\tau<0$, the RFWM spectrum becomes completely independent of τ, and $R \approx 3$ at $\Delta=0$. In the limit of $\gamma \ll \alpha_1, \alpha_3$, we have

$$I(\Delta,\tau) \propto \frac{\gamma}{2\alpha_1} + \frac{\gamma(\alpha_1+\alpha_3)}{(\alpha_1+\alpha_3)^2+\Delta^2} + \left(1-\frac{\gamma}{2\alpha_1} + \frac{2\gamma(\alpha_1+\alpha_3)}{(\alpha_1+\alpha_3)^2+\Delta^2}\right)\exp(-2\alpha_1|\tau|)$$

for $\tau>0$ [Fig. 2(b)], and

$$I(\Delta,\tau) \propto \frac{\gamma}{2\alpha_1} + \frac{\gamma(\alpha_1+\alpha_3)}{(\alpha_1+\alpha_3)^2+\Delta^2} + \left(1-\frac{\gamma}{2\alpha_1} - \frac{2\gamma(\alpha_3-\alpha_1)}{(\alpha_3-\alpha_1)^2+\Delta^2}\right)\exp(-2\alpha_1|\tau|) + \frac{4\gamma\alpha_1\exp[-(\alpha_1+\alpha_3)|\tau|]}{{\alpha_1}^4-2{\alpha_1}^2({\alpha_3}^2-\Delta^2)+({\alpha_3}^2+\Delta^2)^2} \times[({\alpha_1}^2-{\alpha_3}^2+\Delta^2)\cos(\Delta|\tau|)+2\alpha_3\Delta\sin(\Delta|\tau|)]$$

for $\tau<0$ [Fig. 2(c)]. The equation for $\tau>0$ indicates that when $\tau=0$ the nonresonant background is larger than the resonant signal by a factor of $(\alpha_1+\alpha_3)/3\gamma \gg 1$ at $\Delta=0$. However, when $\alpha_i|\tau| \gg 1$ then the resonant signal and the nonresonant background become comparable, and we have $R=2\alpha_1/(\alpha_1+\alpha_3)$, which equals 1 if $\alpha_1=\alpha_3$.

Finally, we have considered the field-correlation effects in a single-relaxation-rate medium for the Gaussian-amplitude model (GAM). In the limit of $\gamma \gg \alpha_1, \alpha_3$ [Fig. 3(a)], we have $I(\Delta,\tau) \propto [1+\exp(-2\alpha_1|\tau|)][1+3\gamma^2/(\gamma^2+\Delta^2)]$ for both $\tau>0$ and $\tau<0$, the RFWM spectrum is independent of τ, and $R \approx 3$ at $\Delta=0$. In the limit of $\gamma \ll \alpha_1, \alpha_3$, we have

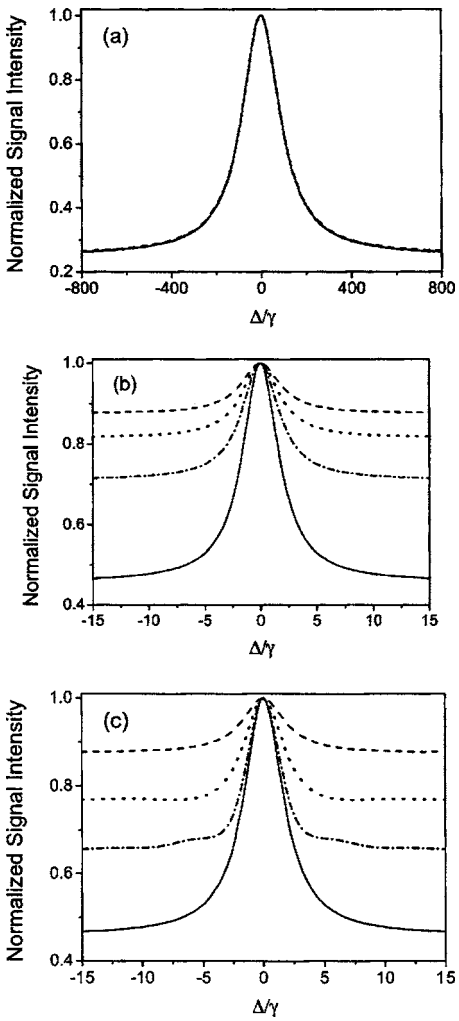

FIG. 2. RFWM spectra versus Δ/γ for the PDM when $\alpha_1\tau=0$ (dashed curve), −0.5 (dotted curve), −1 (dot-dashed curve), −10 (solid curve), $\alpha_3/\alpha_1=1$, $\gamma/\alpha_1=100$ for (a), $\gamma/\alpha_1=0.1$ for (c); $\alpha_1\tau=0$ (dashed curve), 0.5 (dotted curve), 1 (dot-dashed curve), 10 (solid curve), $\alpha_3/\alpha_1=1$, $\gamma/\alpha_1=0.1$ for (b).

$$I(\Delta,\tau) \propto \frac{\gamma}{2\alpha_1} + \frac{\gamma(\alpha_1+\alpha_3)}{(\alpha_1+\alpha_3)^2+\Delta^2} + \left[1+\frac{\gamma}{2\alpha_1} + \frac{2\gamma(\alpha_1+\alpha_3)}{(\alpha_1+\alpha_3)^2+\Delta^2}\right]\exp(-2\alpha_1|\tau|)$$

for $\tau>0$ [Fig. 3(b)], and

$$I(\Delta,\tau) \propto \frac{\gamma}{2\alpha_1} + \frac{\gamma(\alpha_1+\alpha_3)}{(\alpha_1+\alpha_3)^2+\Delta^2} + \left(1+\frac{\gamma}{2\alpha_1} - \frac{2\gamma(\alpha_1-\alpha_3)}{(\alpha_1-\alpha_3)^2+\Delta^2}\right)\exp(-2\alpha_1|\tau|) + \frac{4\gamma\alpha_1\exp[-(\alpha_1+\alpha_3)|\tau|]}{{\alpha_1}^4-2{\alpha_1}^2({\alpha_3}^2-\Delta^2)+({\alpha_3}^2+\Delta^2)^2} \times[({\alpha_1}^2-{\alpha_3}^2+\Delta^2)\cos(\Delta|\tau|)+2\alpha_3\Delta\sin(\Delta|\tau|)]$$

for $\tau<0$ [Fig. 3(c)]. The equation for $\tau>0$ indicates that when $\tau=0$ the nonresonant background is larger than the

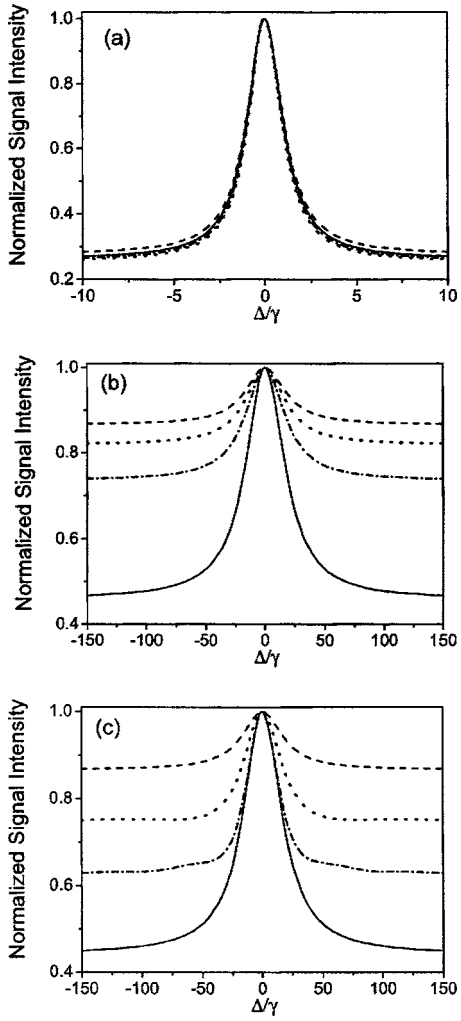

FIG. 3. RFWM spectra versus Δ/γ for the GAM when $\alpha_1\tau=0$ (dashed curve), −0.5 (dotted curve), −1 (dot-dashed curve), −10 (solid curve), $\alpha_3/\alpha_1=1$, $\gamma/\alpha_1=10$ for (a), $\gamma/\alpha_1=0.1$ for (c); $\alpha_1\tau=0$ (dashed curve), 0.5 (dotted curve), 1 (dot-dashed curve), 10 (solid curve), $\alpha_3/\alpha_1=1$, $\gamma/\alpha_1=0.1$ for (b).

resonant signal by a factor of $(\alpha_1+\alpha_3)/3\gamma \gg 1$ at $\Delta=0$. However, when $\alpha_i|\tau| \gg 1$ then the resonant signal and the nonresonant background become comparable, and we have $R=2\alpha_1/(\alpha_1+\alpha_3)$, which equals 1 if $\alpha_1=\alpha_3$.

B. Absorbing medium with two relaxation rates of the molecular-reorientational grating and the thermal grating

The difference in the temporal behavior of the RFWM for $\gamma_2 \gg \alpha_1$, α_3 and $\gamma_1 \ll \alpha_1, \alpha_3$ can be employed for the suppression of nonresonant thermal background in an absorbing medium (with the nonlinear susceptibilities χ_1 and χ_2, and the relaxation rates γ_1 and γ_2 for the thermal grating and the molecular-reorientational grating, respectively). For simplicity, here we consider the limits $\gamma_2 \gg \alpha_1, \alpha_3 \gg \gamma_1$ for the CFM; then we have for $\tau=0$,

$$I(\Delta) \propto \chi_1^{\,2} + 2\chi_2^{\,2}\left(1+\frac{3\gamma_2^{\,2}}{\gamma_2^{\,2}+\Delta^2}\right) + 2\chi_1\chi_2\left(1+\frac{\gamma_2^{\,2}}{\gamma_2^{\,2}+\Delta^2}\right);$$

whereas in the limit of $|\tau| \to \infty$,

$$I(\Delta) \propto \chi_1^{\,2}\left(\frac{\gamma_1}{2\alpha_1}+\frac{\gamma_1(\alpha_1+\alpha_3)}{(\alpha_1+\alpha_3)^2+\Delta^2}\right) + \chi_2^{\,2}\left(1+\frac{3\gamma_2^{\,2}}{\gamma_2^{\,2}+\Delta^2}\right).$$

Suppose that the thermal grating is much more efficient than the molecular-reorientational grating so that $\chi_1^{\,2} \gg \chi_2^{\,2}$, then we have $I(\Delta) \propto \chi_1^{\,2}$ at zero time delay. Hence, the RFWM spectrum is dominated by the nonresonant thermal background. The contribution from the thermal grating can be reduced significantly as we increase the time delay between beams 1 and 2. When beams 1 and 2 become completely uncorrelated, the condition for the suppression of nonresonant thermal background is $(\chi_1/\chi_2)^2(\gamma_1/2\alpha_1) \ll 1$. In this case, we have $I(\Delta) \propto \chi_2^{\,2}[1+/3\gamma_2^{\,2}/(\gamma_2^{\,2}+\Delta^2)]$, which is exactly the RFWM spectrum of a sample with molecular-reorientational grating alone.

Next we consider the limits $\gamma_2 \gg \alpha_1, \alpha_3 \gg \gamma_1$ for the PDM and GAM. We have

$$I(\Delta) \propto \chi_1^{\,2} + \chi_2^{\,2}\left(1+\frac{3\gamma_2^{\,2}}{\gamma_2^{\,2}+\Delta^2}\right) + 2\chi_1\chi_2\left(1+\frac{\gamma_2^{\,2}}{\gamma_2^{\,2}+\Delta^2}\right)$$

for $\tau=0$ of the PDM (Fig. 4), and

$$I(\Delta) \propto \chi_1^{\,2} + 3\chi_2^{\,2}\left(1+\frac{3\gamma_2^{\,2}}{\gamma_2^{\,2}+\Delta^2}\right) + 2\chi_1\chi_2\left(1+\frac{\gamma_2^{\,2}}{\gamma_2^{\,2}+\Delta^2}\right)$$

for $\tau=0$ of the GAM (Fig. 5), respectively. Suppose that the thermal grating is much more efficient than the molecular-reorientational grating so that $\chi_1^{\,2} \gg \chi_2^{\,2}$, then we have $I(\Delta) \propto \chi_1^{\,2}$ at zero time delay. Hence, the RFWM spectrum is dominated by the nonresonant thermal background. At zero delay time it shows the drastic difference for three Markovian stochastic fields for $\gamma_2 \gg \alpha_1$, $\alpha_3 \gg \gamma_1$ approximation. On the other hand, the PDM and GAM results are the same as those of the CFM in the limit of $|\tau| \to \infty$ (Fig. 6). The contribution from the thermal grating can also be reduced significantly as we increase the time delay between beams 1 and 2.

In nonresonant RFWM, the thermal effect of an absorbing medium can be suppressed by a time-delayed method. The resonant signal and the nonresonant background originate from the order parameters $Q_3(\mathbf{r},t)$ and $Q_1(\mathbf{r},t)$, respectively. According to Eqs. (7) and (9), integration effects are involved in the establishment of order parameters of the gratings. Considering the broadband noisy-light case (i.e., $\gamma \ll \alpha_1, \alpha_3$), the effect of integration is to wash out the gratings. At zero time delay no washout takes place in the establishment of $Q_1(\mathbf{r},t)$ because the phase factor ϕ_1 of $A_1(t-t') \times [A_1'(t-t')]^*$ is stationary. On the other hand, the phase factor ϕ_3 of $[A_1'(t-t')]^* A_3(t-t')$ is a random variable which fluctuates with a characteristic time scale $(\alpha_1+\alpha_3)^{-1}$. Because of the integration effect, the fast random fluctuation of ϕ_3 leads to the reduction of the amplitude of Q_3. Therefore, the RFWM spectrum is dominated by a large nonresonant background when $\tau=0$. The RFWM spectrum in the limit of $|\tau| \gg 1/\alpha$ is quite different. Similar to Q_3, Q_1 is now induced by mutually incoherent fields. If $\alpha_1=\alpha_3$, then the influences of the integration effect on Q_1 and Q_3 are equal. In the case of $\Delta=0$, the signals from Q_1 and Q_3 will be equal. Furthermore, the relative phase between $P_1(\mathbf{r},t)$ and $P_3(\mathbf{r},t)$ is a

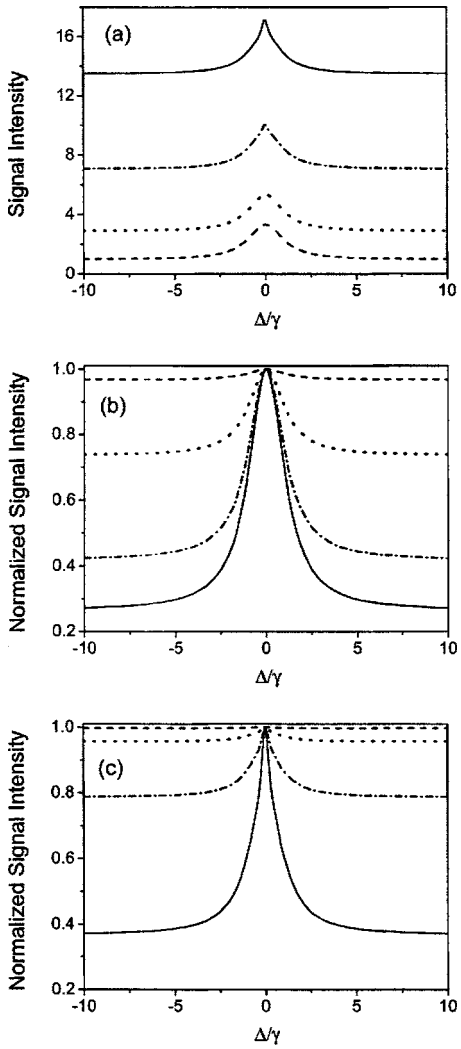

FIG. 4. RFWM spectra of the PDM in an absorbing medium for (a) $\alpha_3/\alpha_1=1$, $\gamma_1/\alpha_1=1\times10^{-5}$, $\gamma_2/\alpha_1=10$, $\alpha_1\tau=-5$, $\chi_1/\chi_2=50$ (dashed curve), 250 (dotted curve), 350 (dot-dashed curve), and 500 (solid curve); (b) $\chi_1/\chi_2=50$, $\alpha_3/\alpha_1=1$, $\gamma_1/\alpha_1=1\times10^{-5}$, $\gamma_2/\alpha_1=10$, $\alpha_1\tau=0$ (dashed curve), −3 (dotted curve), −4 (dot-dashed curve), and −10 (solid curve); (c) $\chi_1/\chi_2=500$, $\alpha_3/\alpha_1=1$, $\gamma_1/\alpha_1=1\times10^{-5}$, $\gamma_2/\alpha_1=10$, $\alpha_1\tau=0$ (dashed curve), −4 (dotted curve), −5 (dot-dashed curve), and −10 (solid curve).

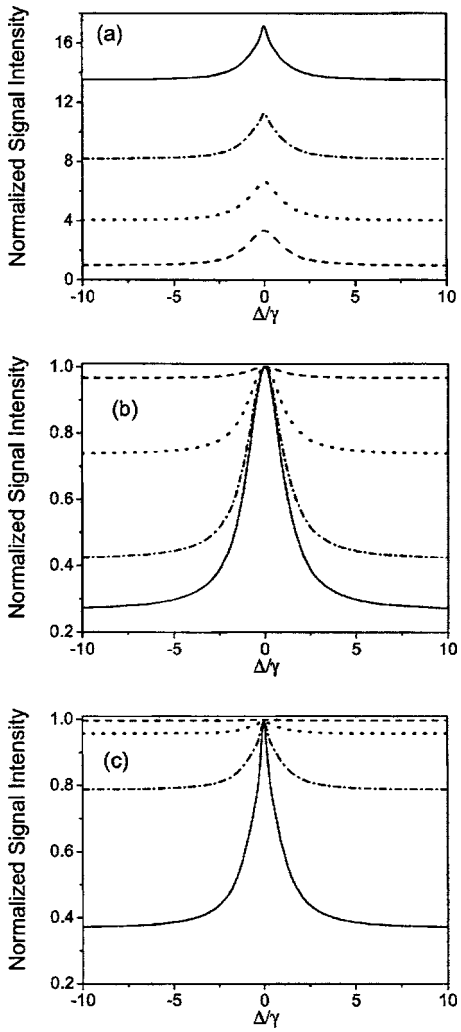

FIG. 5. RFWM spectra of the GAM in an absorbing medium for (a) $\alpha_3/\alpha_1=1$, $\gamma_1/\alpha_1=1\times10^{-5}$, $\gamma_2/\alpha_1=10$, $\alpha_1\tau=-5$, $\chi_1/\chi_2=50$ (dashed curve), 250 (dotted curve), 380 (dot-dashed curve), and 500 (solid curve); (b) $\chi_1/\chi_2=50$, $\alpha_3/\alpha_1=1$, $\gamma_1/\alpha_1=1\times10^{-5}$, $\gamma_2/\alpha_1=10$, $\alpha_1\tau=0$ (dashed curve), −3 (dotted curve), −4 (dot-dashed curve), and −10 (solid curve); (c) $\chi_1/\chi_2=500$, $\alpha_3/\alpha_1=1$, $\gamma_1/\alpha_1=1\times10^{-5}$, $\gamma_2/\alpha_1=10$, $\alpha_1\tau=0$ (dashed curve), −4 (dotted curve), −5 (dot-dashed curve), and −10 (solid curve).

stochastic variable. Since there is no interference between them, we have $R\approx1$, which is defined as the ratio between the intensity of the resonant signal at $\Delta=0$ and the nonresonant background. We now consider the narrow-bandwidth case when $\gamma\gg\alpha_1,\alpha_3$. In this case, the material gratings have very short relaxation times; therefore, they can respond to the phase fluctuations of the fields almost immediately. More specifically, $A_1(t-t')[A_1'(t-t')]^*$ and $[A_1'(t-t')]^*A_3(t-t')$ in Eqs. (7) and (9), respectively, are slowly varying functions in comparison with $\exp(-\gamma t')$ which have a peak at $t'=0$, and therefore can be approximated as $A_1(t)[A_1'(t)]^*$ and $[A_1'(t)]^*A_3(t)$, respectively. We have $P_1(\mathbf{r},t)\propto\chi\gamma A_1(t)\times[A_1'(t)]^*A_3(t)\int_0^\infty\exp(-\gamma t')dt'$ and $P_3(\mathbf{r},t)\propto\chi\gamma A_1(t)\times[A_1'(t)]^*A_3(t)\int_0^\infty\exp[-(\gamma-i\Delta)t']dt'$. These equations indicate that the RFWM spectrum is independent of τ. Although the phases of P_1 and P_3 fluctuate randomly, the relative phase between them is fixed; therefore, we have $R\approx3$ instead of 1 due to the interference between P_1 and P_3.

The fact that the effect of field correlation on the order parameters Q_1 and Q_3 is different. In particular, as we increase the time delay, the phase fluctuation of the interference pattern of beams 1 and 2 affects the establishment of Q_1 directly. In contrast, since Q_3 is induced by beams 2 and 3, the integration effect will not lead directly to the τ dependence of Q_3. The field-correlation effect here is due to the coincidence of the intensity spikes between Q_3 and beam 1 instead. The RFWM is also influenced by the interference between signals originating from Q_1 and Q_3. The degree of the interference is reflected in the parameter $R=I_{\text{res}}(\Delta=0)/I_{\text{nonres}}$. For example, the signal intensities arising from Q_1 and Q_3 are equal in the limit of $|\tau|\to\infty$ when $\alpha_1=\alpha_3$ and $\Delta=0$. However, it can be proved that $R\approx1+2\gamma/(\gamma+\alpha_1)$;

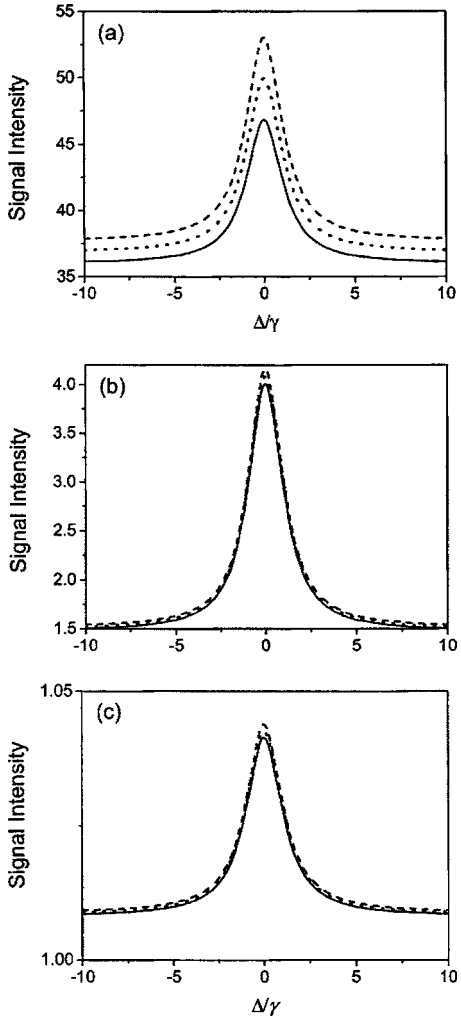

FIG. 6. RFWM spectra in an absorbing medium for (a) $\alpha_3/\alpha_1=1$, $\gamma_1/\alpha_1=1\times10^{-5}$, $\gamma_2/\alpha_1=10$, $\alpha_1\tau=0$, $\chi_1/\chi_2=5$; (b) $\chi_1/\chi_2=5$, $\alpha_3/\alpha_1=1$, $\gamma_1/\alpha_1=1\times10^{-5}$, $\gamma_2/\alpha_1=10$, $\alpha_1\tau=-2$; (c) $\chi_1/\chi_2=50$, $\alpha_3/\alpha_1=1$, $\gamma_1/\alpha_1=1\times10^{-5}$, $\gamma_2/\alpha_1=10$, $\alpha_1\tau=0$. The three curves represent the chaotic field (dotted line), phase-diffusion field (solid line), and Gaussian-amplitude field (dashed line), respectively. The three curves in (c) have been decreased by a factor of 2580.

therefore, the contribution from the interference term is given by $2\gamma/(\gamma+\alpha_1)$, which varies from 0 for $\alpha_1 \gg \gamma$ to 2 for $\alpha_1 \ll \gamma$ (see Figs. 2 and 3).

Based on the field-correlation effects, the thermal grating can be suppressed by a time-delayed method. This method employs the intrinsic incoherence of laser beams and the order-of-magnitude difference between the relaxation time of the molecular reorientational grating and the thermal grating. Consider a RFWM in an absorbing sample. Because of the high efficiency of thermal effects, then similar to Figs. 4–6 the Rayleigh-type FWM spectrum will exhibit a large nonresonant background when $\tau=0$. The nonresonant background can be reduced if we increase the relative time delay between beams 1 and 2. A reduction factor of $2\alpha_1/\gamma_T$ can be achieved when beams 1 and 2 become uncorrelated. The residue thermal effects can be reduced further if we use pump beams with broader linewidth and/or longer pulse width. In addition, this method will not affect the strict phase-matching condition, because beams 1 and 2 originate from a single laser source, and therefore they have the same frequency even though they become completely uncorrelated. Typically, the relaxation time of a thermal grating is on the order of a microsecond. Letting $\alpha_1 \approx 0.1\gamma_M$ and assuming that the relaxation time of the molecular-reorientational grating is a few hundreds of femtoseconds, the reduction factor is about 10^{-6}. If we employ pulse lasers with pulse width smaller than the relaxation time of the thermal grating, then due to the finite interaction time between the laser and the material, the role of the relaxation time should be replaced by the laser pulse width. For a laser pulse width of 5 ns, the reduction factor becomes 10^{-5}. On the other hand, in contrast to the thermal grating, the field correlation has little influence on the RFWM spectrum when the grating has a fast relaxation time. Therefore, the ultrafast longitudinal relaxation time can be measured even in an absorbing medium [7]. Using a similar idea, the hidden Raman resonance can be revealed from the thermal background by a time-delayed method in Raman-enhanced FWM experiments [17,18].

As a nonlinear spectroscopy, the most important question in RFWM is the "frequency bandwidth," or, equivalently, the avoidance of phase mismatch during wavelength tuning. The coherence length in RFWM is given by $l_c=2c/[n(\omega_1/\omega_3)|\omega_1-\omega_3|\theta^2]$, where n is the refractive index. To ensure that the phase mismatching does not affect the experimental results, the coherence length l_c must be larger than the thickness of the sample cell. The frequency bandwidth can be increased further by reducing the angle between beams 1 and 2; therefore, in principle, relaxation times shorter than 10 fs can be measured. In coherent Raman spectroscopy the spectrum usually exhibits an asymmetric line shape, because of the interference between the resonant signal and the nonresonant background. In contrast, RFWM is a nonresonant process, and the line shape is symmetric even though interference between signals from two gratings exists. Finally, although several frequency-domain nonlinear laser spectroscopies have been suggested for ultrafast measurements [7], RFWM possesses the following features. It involves three incident beams; therefore, different tensor components of the nonlinear susceptibility can be measured independently. The angle between beams 1 and 2 can be adjusted for individual experiments to optimize the tradeoff between better phase matching and larger interaction volume or better spatial resolution. The RFWM signal is coherent light, which makes it easier to detect.

One interesting feature in field-correlation effects is that RFWM exhibits temporal asymmetry and spectral symmetry. Beam 1 is used to probe the moving grating Q_3, which decays with rate γ. The γ dependence in the temporal behavior of $I(\Delta,\tau)$ for $\tau<0$ is the result of the amplitude correlation between beam 1 and Q_3. More specifically, according to Eqs. (7) and (9), $I(\Delta,\tau)$ is asymmetric in τ in general because it only depends on the laser coherence time when $\tau>0$, while it depends on both the laser coherence time and the relaxation time of the grating when $\tau<0$ for chaotic fields (Fig. 7). The maximum of the temporal profile for RFWM is shifted from $\tau=0$. The maximum position is almost same in curve (a) of $|\langle P_3\rangle|^2$ and curve (b) of $\langle|P_3|^2\rangle$ (Fig. 7). The τ-dependent main terms all show in the $|\langle P_3\rangle|^2$ case. Physi-

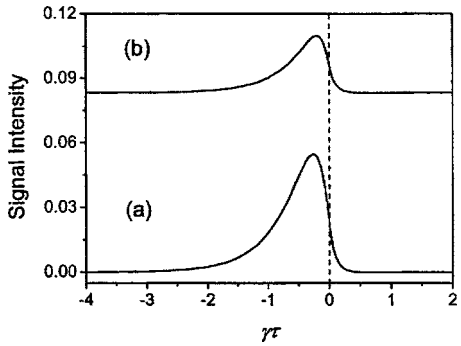

FIG. 7. RFWM signal comparison of $|\langle P_3\rangle|^2$, curve (a), and $\langle|P_3|^2\rangle$ for the CFM, curve (b) versus time delay $\gamma\tau$. The parameters are $\alpha_1/\gamma=5.6$, $\alpha_3/\gamma=5.4$, and $\Delta/\gamma=0$.

cally, RFWM is similar to the corresponding CSRS. Unlike CSRS no coherence spike appears at $\tau=0$. As the laser linewidth α_1/γ increases, the maximum is closer to $\tau=0$, and the τ-independent nonresonant background is increased. Moreover, the terms $\langle P_3 P_3^{*}\rangle$ (interference from purely Rayleigh-resonant signals) and $\langle P_1 P_3^{*}\rangle$ and $\langle P_1^{*} P_3\rangle$ (interference between the Rayleigh-resonant signal and the nonresonant background) of RFWM exhibits hybrid radiation-matter detuning terahertz damping oscillation. On the other hand, unlike the Raman-enhanced FWM spectrum, which is asymmetric due to the interference between the resonant signal and the nonresonant background [17,18], the line shape of the Rayleigh-type FWM is always symmetric. Specifically, in Raman-enhanced FWM the Raman vibration is excited by the simultaneous presence of two incident beams whose frequency difference equals the Raman excitation frequency and the Raman-enhanced FWM signal is the result of this resonant excitation. In contrast, Rayleigh-type FWM is a nonresonant process with no energy transfer between the light and the medium when the frequency difference between two incident beams equals zero. The resonant structure in the Rayleigh-type FWM spectrum is the result of an induced moving grating. This difference is also reflected in their line shapes. This symmetry is manifested in the RFWM spectrum. The RFWM spectrum shows a smooth curve when $\tau>0$ [see Figs. 2(b) and 3(b)], while it exhibits a wavelike structure when $\alpha\tau=-0.5$ or -1 for three different Markovian stochastic fields in Figs. 2(c) and 3(c). The wavelike structure originates from $\sin(\Delta\tau)$ and $\cos(\Delta\tau)$ in Eq. (12), which describes the interference between signals from order parameters Q_1 and Q_3.

Comparing with the CFM and GAM, due to the absence of single $\exp(-2\alpha_1|\tau|)$ decay factors (which comes from the amplitude fluctuation) in the PDM [17,18], the RFWM spectrum for PDM shows the broadest line shape in the narrowband case [Fig. 8(a)], and extremely narrow line shape in the broadband linewidth, respectively [Fig. 8(b)].

IV. HOMODYNE DETECTION OF SUM-FREQUENCY RASPB

We have the total third-order polarization $P^{(3)}=P_1+P_2+P_3$. For the macroscopic system where phase matching

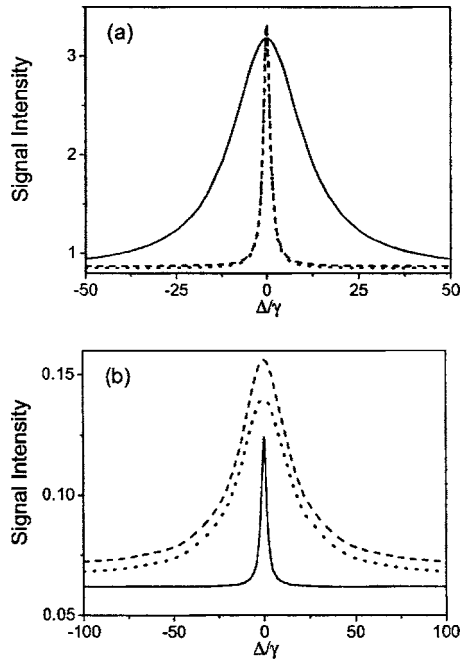

FIG. 8. RFWM spectra versus $\Delta/\gamma\cdot\alpha_3/\alpha_1=1$, $\alpha_1\tau=-2$, $\gamma/\alpha_1=10$ for (a) and $\gamma/\alpha_1=0.1$ for (b). The three curves represent the chaotic field (dotted line), phase-diffusion field (solid line), and Gaussian-amplitude field (dashed line), respectively.

takes place this signal must be drawn from the $P^{(3)}$ developed on one chromophore multiplied by the $(P^{(3)})^{*}$ that is developed on another chromophore which must be located elsewhere in space (with summation over all such pairs) [8–16]. The bichromophoric model is particularly important to noisy light spectroscopies where stochastic averaging at the signal level must be carried out. The sum-frequency RASPB signal is proportional to the average of the absolute square of $P^{(3)}$ over the random variable of the stochastic process, so that the signal $I(\Delta,\tau)\propto\langle|P^{(3)}|^2\rangle=\langle P^{(3)}(P^{(3)})^{*}\rangle=\langle(P_1+P_2+P_3)[(P_1)^{*}+(P_2)^{*}+(P_3)^{*}]\rangle$ contains $3\times3=9$ different terms in the fourth- and second-order coherence functions of $u_i(t)$ in phase-conjugation geometry. In general, the RASPB of homodyne detection (at this intensity level) can be viewed as built of the sum of three contributions: (i) the τ-independent or -dependent nonresonant autocorrelation terms of ω_2 molecular-reorientational grating, which include $u_2(t)$ fourth-order and $u_3(t)$ second-order Markovian stochastic correlation functions; (ii) the τ-independent or -dependent autocorrelation terms (i.e., RFWM) of the ω_1 nonresonant molecular-reorientational grating and $|\omega_3-\omega_1|=\Delta$ Rayleigh resonant mode, which include $u_1(t)$ fourth-order and $u_3(t)$ second-order Markovian stochastic correlation functions; (iii) the τ-dependent cross-correlation terms between RFWM and NDFWM processes, which include $u_1(t)$, $u_2(t)$, and $u_3(t)$ second-order Markovian stochastic correlation functions. Different Markovian stochastic models of the laser field affect only the fourth-, not the second-order correlation functions.

A. Analytic closed form for chaotic field

We first assumed that the laser sources are chaotic fields. A chaotic field, which is used to describe a multimode laser

source, is characterized by the fluctuation of both the amplitude and the phase of the field. The random functions $u_i(t)$ of the complex noisy fields are taken to obey complex Gaussian statistics with its fourth-order coherence function satisfying [27]

$$\langle u_i(t_1)u_i(t_2)u_i^*(t_3)u_i^*(t_4)\rangle = \langle u_i(t_1)u_i^*(t_3)\rangle\langle u_i(t_2)u_i^*(t_4)\rangle + \langle u_i(t_1)u_i^*(t_4)\rangle\langle u_i(t_2)u_i^*(t_3)\rangle. \tag{10}$$

All higher-order coherence functions can be expressed in terms of products of second-order coherence functions. Thus any given $2n$-order coherence function may be decomposed into a sum of $n!$ terms, each consisting of the products of n second-order coherence functions.

The composite noisy beam 1 (beam 2) is treated as one whose spectrum is simply a sum of two Lorentzians. The high-order decay cross-correlation terms are reasonably neglected in our treatment. After substituting Eq. (10) into $I(\Delta,\tau)\propto\langle|P^{(3)}|^2\rangle$ and performing the tedious integration, we obtain for (i) $\tau>0$,

$$I(\Delta,\tau)\propto\chi^2\left[\frac{\gamma}{\gamma+2\alpha_1}+\frac{\eta^2\gamma}{\gamma+2\alpha_2}+\frac{\gamma_a\gamma}{\gamma_a^2+\Delta^2}+\frac{(\gamma+\gamma_a)\gamma^2}{(\gamma+\alpha_1)[(\gamma_a+\gamma)^2+\Delta^2]}+\frac{2[\gamma_a(\gamma+\gamma_a)-\Delta^2]\gamma^2}{(\gamma_a^2+\Delta^2)[(\gamma_a+\gamma)^2+\Delta^2]}\right.$$
$$+\left(1+\frac{2\gamma_a\gamma}{\gamma_a^2+\Delta^2}+\frac{\gamma_a\gamma^2}{(\gamma+\alpha_1)(\gamma_a^2+\Delta^2)}\right)\exp(-2\alpha_1|\tau|)+\eta^2\exp(-2\alpha_2|\tau|)$$
$$\left.+\eta\left(A+A^*+\frac{A\gamma}{\gamma_a-i\Delta}+\frac{A^*\gamma}{\gamma_a+i\Delta}\right)\exp[-(\alpha_1+\alpha_2)|\tau|]\right], \tag{11}$$

and for (ii) $\tau<0$,

$$I(\Delta,\tau)\propto\chi^2\left\{\frac{\gamma}{\gamma+2\alpha_1}+\frac{2\gamma^2(\gamma+\gamma_a)}{(\gamma+2\alpha_1)[(\gamma_a+\gamma)^2+\Delta^2]}+\frac{2\gamma^2(2\gamma^2-\Delta^2+3\gamma\alpha_1+\alpha_1^2+3\gamma\alpha_3+2\alpha_1\alpha_3+\alpha_3^2)}{(\gamma_a^2+\Delta^2)[(\gamma_a+\gamma)^2+\Delta^2]}+\frac{\gamma\gamma_a}{\gamma_a^2+\Delta^2}\right.$$
$$+\frac{\eta^2\gamma}{\gamma+2\alpha_2}-\frac{2\gamma\alpha_1(\gamma+\gamma_c+i\Delta)}{(\gamma_c+i\Delta)(\gamma_b-i\Delta)(\gamma_a-i\Delta)}\exp[-(\gamma_a-i\Delta)|\tau|]-\frac{2\gamma\alpha_1(\gamma+\gamma_c-i\Delta)}{(\gamma_c-i\Delta)(\gamma_b+i\Delta)(\gamma_a+i\Delta)}\exp[-(\gamma_a+i\Delta)|\tau|]$$
$$+\frac{2\gamma^2\alpha_1(2\gamma^2\alpha_1-2\alpha_1^3+\gamma^2\alpha_3-\Delta^2\alpha_3-5\alpha_1^2\alpha_3-4\alpha_1\alpha_3^2-\alpha_3^3)}{(\gamma^2-\alpha_1^2)(\gamma_c^2+\Delta^2)(\gamma_a^2+\Delta^2)}\exp(-2\gamma|\tau|)+\left[1+\left(2+\frac{\gamma}{\gamma-\alpha_1}\right)\frac{\gamma\gamma_b}{\gamma_b^2+\Delta^2}\right]$$
$$\times\exp(-2\alpha_1|\tau|)+\eta^2\exp(-2\alpha_2|\tau|)-\frac{2\gamma\alpha_1A\eta\exp[-(\gamma_a-i\Delta)|\tau|]}{(\gamma_b-i\Delta)(\gamma_a-i\Delta)}-\frac{2\gamma\alpha_1A^*\eta\exp[-(\gamma_a+i\Delta)|\tau|]}{(\gamma_b+i\Delta)(\gamma_a+i\Delta)}$$
$$\left.+\eta\left(\frac{A^*\gamma}{\gamma_b+i\Delta}+\frac{A\gamma}{\gamma_b-i\Delta}+A+A^*\right)\exp[-(\alpha_1+\alpha_2)|\tau|]\right\}. \tag{12}$$

Here, $\eta=\varepsilon_2'\varepsilon_2/\varepsilon_1'\varepsilon_1$ (assuming $\varepsilon_1'\approx\varepsilon_1$ and $\varepsilon_2'\approx\varepsilon_2$); $\Delta\mathbf{k}=(\mathbf{k}_1-\mathbf{k}_1')-(\mathbf{k}_2'-\mathbf{k}_2)$; $\gamma_a=\gamma+\alpha_1+\alpha_3$, $\gamma_b=\gamma-\alpha_1+\alpha_3$, $\gamma_c=\gamma-\alpha_1-\alpha_3$; $A=\exp[i\Delta\mathbf{k}\cdot\mathbf{r}-i(\omega_1+\omega_2)\tau]=\exp(i\theta)$.

In general $I(\Delta,\tau)$ is asymmetric in τ because it depends only on the laser coherence time when $\tau>0$, while it depends on both the laser coherence time and the relaxation time of the grating when $\tau<0$. The RASPB is generally different for $\tau>0$ and $\tau<0$. Even when $|\tau|\to\infty$, Eq. (11) is still different from Eq. (12). In general the RASPB depends only on the laser coherence time when $\tau>0$, while it depends on both the laser coherence time and the relaxation time of the grating (which decays with rate γ) when $\tau<0$. Different Markovian stochastic models of the laser field affect only the fourth-, not the second-order correlation functions. The interferometric contrast ratio of the interferogram mainly determined by the cross-correlation between RFWM and NDFWM processes is equally sensitive to the amplitude and phase fluctuations of the chaotic fields. The constant term $\chi^2\gamma\gamma_a/(\gamma_a^2+\Delta^2)$ in relations (11) and (12), which is independent of the relative time delay between twin beams 1 and 2, originates from the phase fluctuation of the chaotic fields, while the purely decay terms including the factors $\exp(-2\alpha_1|\tau|)$, $\exp(-2\alpha_2|\tau|)$, and $\exp(-2\gamma|\tau|)$ in relations (11) and (12) come from amplitude fluctuation of the chaotic fields. Physically, the chaotic field has the property of photon bunching, which can affect any multiphoton process when the higher-order correlation function of the field plays an important role. Based on the chaotic field, the resonant autocorrelation between the Rayleigh-active modes [i.e., a factor $\exp(-2\gamma|\tau|)$ which originates from the $\langle P_3P_3^*\rangle$ term] is shown in Eq. (12) for $\tau<0$.

The characteristics of the interferogram of the RASPBs are a result of two main components: the material response (resonant term) and the light response (nonresonant term) along with the interplay between the two responses. Equations (11) and (12) generally indicate not only the characteristic of twin laser fields, but also a molecule vibrational property. Specifically, the temporal behaviors of the sum-frequency RASPB intensities mainly reflect the characteristics of twin composite laser fields for $\tau>0$, and the molecule vibrational properties for $\tau<0$. The sum-frequency RASPB signal versus τ typically shows the attosecond scale modulation with a sum frequency $\omega_2+\omega_1$ and a damping rate $\alpha_1+\alpha_2$. If we employ sum-frequency RASPB on the attosecond scale to measure the modulation frequency $\omega_s=\omega_2+\omega_1$, the accuracy can be improved by measuring as many cycles of the attosecond modulation as possible. Since the amplitude of the attosecond modulation decays with a time constant $(\alpha_1+\alpha_2)^{-1}$ as $|\tau|$ increases, the maximum domain of time delay $|\tau|$ should equal approximately $2(\alpha_1+\alpha_2)^{-1}$. We obtain the theoretical limit of the uncertainty of the modulation frequency measurement $\Delta\omega_s$ which is $\Delta\omega_s \approx \pi(\alpha_1+\alpha_2)$, i.e., in the modulation frequency measurement the theoretical limit of the accuracy is related to the decay time constant of the beat signal modulation amplitude.

Equations (11) and (12) indicate that the beat signal oscillates not only temporally but also spatially with a period $2\pi/\Delta k$ along the direction $\Delta\mathbf{k}$, which is almost perpendicular to the propagation direction of the beat signal. Here $\Delta k \approx 2\pi|\lambda_1-\lambda_2|\theta/\lambda_2\lambda_1$, where θ is the angle between beam 1 and beam 2. Physically, the polarization-beat model assumes that the twin composite beams are plane waves. Therefore the RFWM and NDFWM signals, which propagate along $\mathbf{k}_1-\mathbf{k}_1'+\mathbf{k}_3$ and $\mathbf{k}_2'-\mathbf{k}_2+\mathbf{k}_3$, respectively, are plane waves also. Since FWM signals propagate along slightly different direction, the interference between them leads to the spatial oscillation. To observe the spatial modulation of the beat signal the dimension of the detector should be smaller than 0.6 mm, which should be detected by pinhole detector. The finite thickness of the sample has a catastrophic effect on the correlation of counterpropagating color-locked noisy fields. Although transverse modulation of the attosecond RASPB signal is considered, the effect of signal integration in the longitudinal direction is reasonably neglected here.

The three-order polarization [see Eqs. (7)–(9)], which involves the integration of t' from 0 to ∞, are the accumulation of the polarization induced at a different time. The RASPB signal exhibits $\omega_2+\omega_1$ ultrafast modulation on the attosecond scale, and the symmetric line shape of the RFWM is good for tuning $\omega_3-\omega_1$ to zero-frequency resonance. Specifically, the relative phase between P_1 and P_3 is now a stochastic variable. Due to the randomization of the relative phase between the Rayleigh resonant term from P_3 and the nonresonant background from P_1 the interference between them disappears almost completely. As a result, the RFWM spectrum exhibits a symmetric line shape (Figs. 2–6). Comparing with the CFM broadband case, the maximum of the RASPB signal in the time [Fig. 9(a)] or frequency domain [Fig. 9(b)] has been shifted back and forth from $\tau=0$ or $\Delta=0$ in the CFM narrow bandwidth.

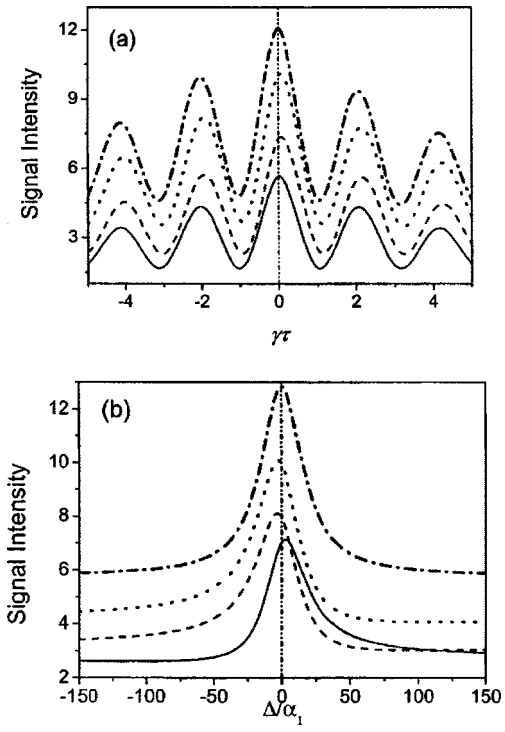

FIG. 9. (a) RASPB signal versus $\gamma\tau$ for $\alpha_1/\gamma=\alpha_2/\gamma=\alpha_3/\gamma=0.1$, $\eta=1$, $r=0$, $\Delta/\alpha_1=0$ (dot-dashed curve), 8 (dotted curve), 20 (dashed curve), and 200 (solid curve); (b) RASPB spectra for $\alpha_1/\gamma=\alpha_2/\gamma=0.06$, $\alpha_3/\gamma=0.05$, $\eta=1$, $r=0$, $\gamma\tau=0$ (dot-dashed curve), -1 (dotted curve), -1.5 (dashed curve), and -2.4 (solid curve).

B. The phase-diffusion field

We have assumed that the laser sources are chaotic field in the above calculation. A chaotic field, which is used to describe a multimode laser source, is characterized by the fluctuation of both the amplitude and the phase of the field. Another commonly used stochastic model is the phase-diffusion model, which is used to describe an amplitude-stabilized laser source. This model assumes that the amplitude of the laser field is a constant, while its phase fluctuates as random process. If the lasers have Lorentzian line shape, the fourth-order coherence function is [27]

$$\langle u_i(t_1)u_i(t_2)u_i^*(t_3)u_i^*(t_4)\rangle = \exp[-\alpha_i(|t_1-t_3|+|t_1-t_4|+|t_2-t_3|+|t_2-t_4|)]\exp[\alpha_i(|t_1-t_2|+|t_3-t_4|)]. \quad (13)$$

After substituting Eq. (13) into $I(\Delta,\tau)\propto\langle|P^{(3)}|^2\rangle$, we obtain, for (i) $\tau>0$,

$$I(\Delta,\tau)\propto\chi^2\Bigg[\frac{\gamma}{\gamma+2\alpha_1}+\frac{\gamma_a\gamma}{{\gamma_a}^2+\Delta^2}+\frac{2(\gamma+\gamma_a)\gamma^2}{(\gamma+2\alpha_1)[(\gamma_a+\gamma)^2+\Delta^2]}+\frac{2[\gamma_a(\gamma+\gamma_a)-\Delta^2]\gamma^2}{({\gamma_a}^2+\Delta^2)[(\gamma_a+\gamma)^2+\Delta^2]}+\frac{\eta^2\gamma}{\gamma+2\alpha_2}$$
$$+\frac{2\alpha_1(3\gamma^2+4\gamma\gamma_a+{\gamma_a}^2+\Delta^2)}{(\gamma+2\alpha_1)({\gamma_a}^2+\Delta^2)}\exp[-(\gamma+2\alpha_1)|\tau|]+\frac{2\eta^2\alpha_2\exp[-(\gamma+2\alpha_2)|\tau|]}{\gamma+2\alpha_2}$$
$$+\eta\left(A+A^*+\frac{A\gamma}{\gamma_a-i\Delta}+\frac{A^*\gamma}{\gamma_a+i\Delta}\right)\exp[-(\alpha_1+\alpha_2)|\tau|]\Bigg], \tag{14}$$

and for (ii) $\tau<0$,

$$I(\Delta,\tau)\propto\chi^2\Bigg[\frac{\gamma}{\gamma+2\alpha_1}+\frac{\gamma\gamma_a}{{\gamma_a}^2+\Delta^2}+\frac{2\gamma^2(\gamma+\gamma_a)}{(\gamma+2\alpha_1)[(\gamma_a+\gamma)^2+\Delta^2]}+\frac{2(\gamma\gamma_a+{\gamma_a}^2-\Delta^2)}{({\gamma_a}^2+\Delta^2)[(\gamma_a+\gamma)^2+\Delta^2]}+\frac{\eta^2\gamma}{\gamma+2\alpha_2}$$
$$+\left(\frac{2\alpha_1}{\gamma+2\alpha_1}+\frac{4\gamma\gamma_b\alpha_1}{({\gamma_b}^2+\Delta^2)(\gamma+2\alpha_1)}\right)\exp[-(\gamma+2\alpha_1)|\tau|]+\frac{2\eta^2\alpha_2\exp[-(\gamma+2\alpha_2)|\tau|]}{\gamma+2\alpha_2}$$
$$-\left(\frac{2\gamma\alpha_1A\eta}{\gamma_b-i\Delta}+\frac{2\gamma\alpha_1}{\gamma+2\alpha_1+\gamma_a-i\Delta}\right)\frac{\exp[-(\gamma_a-i\Delta)|\tau|]}{\gamma_a-i\Delta}-\left(\frac{2\gamma\alpha_1A^*\eta}{\gamma_b+i\Delta}+\frac{2\gamma\alpha_1}{\gamma+2\alpha_1+\gamma_a+i\Delta}\right)\frac{\exp[-(\gamma_a+i\Delta)|\tau|]}{\gamma_a+i\Delta}$$
$$-\left(\frac{2}{\gamma_b-i\Delta}+\frac{\gamma\exp[-(2\alpha_1+\gamma_a-i\Delta)|\tau|]}{(\gamma_a-i\Delta)(2\alpha_1+\gamma_a+\gamma-i\Delta)}\right)\frac{4\gamma{\alpha_1}^2\exp[-(\gamma+\gamma_a-i\Delta)|\tau|]}{(\gamma_a+\gamma-i\Delta)(2\alpha_1+\gamma_a-i\Delta)}-\left(\frac{2}{\gamma_b+i\Delta}+\frac{\gamma\exp[-(2\alpha_1+\gamma_a+i\Delta)|\tau|]}{(\gamma_a+i\Delta)(2\alpha_1+\gamma_a+\gamma+i\Delta)}\right)$$
$$\times\frac{4\gamma{\alpha_1}^2\exp[-(\gamma+\gamma_a+i\Delta)|\tau|]}{(\gamma_a+\gamma+i\Delta)(2\alpha_1+\gamma_a+i\Delta)}+\eta\left(\frac{A^*\gamma}{\gamma_b+i\Delta}+\frac{A\gamma}{\gamma_b-i\Delta}+A+A^*\right)\exp[-(\alpha_1+\alpha_2)|\tau|]\Bigg]. \tag{15}$$

Equations (14) and (15) depend on both the laser coherence time and the relaxation time of the grating. The temporal behavior of the beat signal reflects not only the characteristic of the lasers, but also the molecule vibrational properties. Equations (14) and (15) are remarkably different from the result based on a chaotic model. Equations (14) and (15) are short of the purely autocorrelation decay terms including the factors $\exp(-2\alpha_1|\tau|)$, $\exp(-2\alpha_2|\tau|)$, and $\exp(-2\gamma|\tau|)$, which are shown to be particularly insensitive to the phase fluctuation of the Markovian stochastic light fields. The drastic difference of the results also exists in the higher-order correlation of RASPB when three Markovian stochastic models are employed [11,12].

In the case of α_1, $\alpha_2\ll\gamma$, the phase-diffusion model predicts a damping oscillation of the attosecond sum-frequency RASPB signal around a constant value. We can understand this phenomenon as follows. The interference pattern of the $\omega_1(\omega_2)$ component of the twin composite beams 1 and 2 will be in constant motion with a characteristic time constant ${\alpha_1}^{-1}({\alpha_2}^{-1})$ when $|\tau|$ is much longer than the laser coherence time τ_c. In the case of α_1, $\alpha_2\ll\gamma$, the relaxation time of the molecular-reorientational grating is so short that the induced gratings G1 and G2 always follow the interference pattern, and therefore the beat signal will never decay. On the other hand, the relative phase between G1 and G2 fluctuates randomly, which makes spatial interference between them impossible. In this case the beat signal intensity is simply the summation of the signal intensity originating from G1 and G2. In contrast, the fringes of G1 and G2 are stable when $|\tau|<\tau_c$. The constructive or destructive interference between G1 and G2 enhances or reduces the beat signal and gives rise to the oscillation of the beat signal intensity as τ varies. We note that the main difference between the phase-diffusion model and the chaotic model is that amplitude fluctuation exists in the latter case. When $|\tau|<\tau_c$, the coincidence of the intensity spikes of the two composite beams gives an additional enhancement of the beat signal for the chaotic model.

C. The Gaussian-amplitude field

The Gaussian-amplitude field has a constant phase but its real amplitude undergoes Gaussian fluctuations. The fourth-order coherence function is [27]

$$\langle u_i(t_1)u_i(t_2)u_i(t_3)u_i(t_4)\rangle=\langle u_i(t_1)u_i(t_3)\rangle\langle u_i(t_2)u_i(t_4)\rangle+\langle u_i(t_1)u_i(t_4)\rangle\langle u_i(t_2)u_i(t_3)\rangle+\langle u_i(t_1)u_i(t_2)\rangle\langle u_i(t_3)u_i(t_4)\rangle. \tag{16}$$

Based on the Gaussian-amplitude field, the high-order decay cross-correlation terms have been reasonably neglected. After substituting Eq. (16) into $I(\Delta,\tau)\propto\langle|P^{(3)}|^2\rangle$, we obtain as follows: (i) for $\tau>0$,

$$I(\Delta,\tau) \propto \chi^2\Bigg[\frac{\gamma}{\gamma+2\alpha_1} + \frac{\eta^2\gamma}{\gamma+2\alpha_2} + \frac{2\gamma_a\gamma}{\gamma_a{}^2+\Delta^2} + \frac{(\gamma+\gamma_a)\gamma^2}{(\gamma+\alpha_1)[(\gamma_a+\gamma)^2+\Delta^2]} + \frac{2[\gamma_a(\gamma+\gamma_a)-\Delta^2]\gamma^2}{(\gamma_a{}^2+\Delta^2)[(\gamma_a+\gamma)^2+\Delta^2]}$$
$$+\left(\frac{\gamma}{\gamma+2\alpha_1}-1-\frac{4(\gamma+\gamma_a)\gamma\alpha_1}{[(\gamma+\gamma_a)^2+\Delta^2](\gamma+2\alpha_1)}\right)\exp[-(\gamma+2\alpha_1)|\tau|]+\left(\frac{\eta^2\gamma}{\gamma+2\alpha_2}-\eta^2\right)\exp[-(\gamma+2\alpha_2)|\tau|]$$
$$+\left(2+\frac{4\gamma_a\gamma}{\gamma_a{}^2+\Delta^2}+\frac{\gamma^2\gamma_a}{(\gamma+\alpha_1)(\gamma_a{}^2+\Delta^2)}\right)\exp(-2\alpha_1|\tau|)+2\eta^2\exp(-2\alpha_2|\tau|)$$
$$+\eta\left(A+A^*+\frac{A\gamma}{\gamma_a-i\Delta}+\frac{A^*\gamma}{\gamma_a+i\Delta}\right)\exp[-(\alpha_1+\alpha_2)|\tau|]\Bigg], \tag{17}$$

and (ii) for $\tau<0$,

$$I(\Delta,\tau) \propto \chi^2\Bigg\{ \frac{\gamma}{\gamma+2\alpha_1} + \frac{2\gamma^2(\gamma+\gamma_a)}{(\gamma+2\alpha_1)[(\gamma_a+\gamma)^2+\Delta^2]} + \frac{2\gamma^2(2\gamma^2-\Delta^2+3\gamma\alpha_1+\alpha_1{}^2+3\gamma\alpha_3+2\alpha_1\alpha_3+\alpha_3{}^2)}{(\gamma_a{}^2+\Delta^2)[(\gamma_a+\gamma)^2+\Delta^2]} + \frac{2\gamma\gamma_a}{\gamma_a{}^2+\Delta^2}$$
$$+\frac{\eta^2\gamma}{\gamma+2\alpha_2}-\left(\frac{\gamma+\gamma_c+i\Delta}{\gamma_c+i\Delta}+\frac{\alpha_1}{(\gamma+\gamma_b)-i\Delta}\right)\frac{2\gamma^2\exp[-(\gamma_a-i\Delta)|\tau|]}{(\gamma_b-i\Delta)(\gamma_a-i\Delta)}-\left(\frac{\gamma+\gamma_c-i\Delta}{\gamma_c-i\Delta}+\frac{\alpha_1}{(\gamma+\gamma_b)+i\Delta}\right)$$
$$\times\frac{2\gamma^2\exp[-(\gamma_a+i\Delta)|\tau|]}{(\gamma_b+i\Delta)(\gamma_a+i\Delta)}+\frac{4\gamma^2\alpha_1{}^2\exp[-(3\gamma+2\alpha_3+2i\Delta)|\tau|]}{(\gamma+\gamma_b+i\Delta)(\gamma_b+i\Delta)(\gamma_a+i\Delta)(\gamma+\gamma_a+i\Delta)}$$
$$+\frac{4\gamma^2\alpha_1{}^2\exp[-(3\gamma+2\alpha_3-2i\Delta)|\tau|]}{(\gamma+\gamma_b-i\Delta)(\gamma_b-i\Delta)(\gamma_a-i\Delta)(\gamma+\gamma_a-i\Delta)}$$
$$+\frac{2\gamma^2\alpha_1(2\gamma^2\alpha_1-2\alpha_1{}^3+\gamma^2\alpha_3-\Delta^2\alpha_3-5\alpha_1{}^2\alpha_3-4\alpha_1\alpha_3{}^2-\alpha_3{}^3)}{(\gamma^2-\alpha_1{}^2)(\gamma_c{}^2+\Delta^2)(\gamma_a{}^2+\Delta^2)}\exp(-2\gamma|\tau|)+\left[2+\left(4+\frac{\gamma}{\gamma-\alpha_1}\right)\frac{\gamma\gamma_b}{\gamma_b{}^2+\Delta^2}\right]$$
$$\times\exp(-2\alpha_1|\tau|)+2\eta^2\exp(-2\alpha_2|\tau|)+\left(\frac{\gamma}{\gamma+2\alpha_1}-1-\frac{4\gamma_b\gamma\alpha_1}{(\gamma_b{}^2+\Delta^2)(\gamma+2\alpha_1)}\right)\exp[-(\gamma+2\alpha_1)|\tau|]$$
$$+\left(\frac{\eta^2\gamma}{\gamma+2\alpha_2}-\eta^2\right)\exp[-(\gamma+2\alpha_2)|\tau|]-\frac{2\gamma\alpha_1A\eta\exp[-(\gamma_a-i\Delta)|\tau|]}{(\gamma_b-i\Delta)(\gamma_a-i\Delta)}-\frac{2\gamma\alpha_1A^*\eta\exp[-(\gamma_a+i\Delta)|\tau|]}{(\gamma_b+i\Delta)(\gamma_a+i\Delta)}$$
$$+\eta\left(\frac{A^*\gamma}{\gamma_b+i\Delta}+\frac{A\gamma}{\gamma_b-i\Delta}+A+A^*\right)\exp[-(\alpha_1+\alpha_2)|\tau|]\Bigg\}. \tag{18}$$

Equations (17) and (18) generally indicate not only the characteristic of twin noisy laser fields, but also a molecule vibrational property. Specifically, the temporal behaviors of the sum-frequency RASPB intensities mainly reflect the characteristics of twin composite laser fields for $\tau>0$, and material vibrational properties for $\tau<0$. Based on the Gaussian-amplitude field, the resonant autocorrelation between the Rayleigh-active modes [i.e., a factor $\exp(-2\gamma|\tau|)$ which originates from the $\langle P_3P_3^*\rangle$ term] is shown in Eq. (18) for $\tau<0$. The τ-independent constant background of Gaussian-amplitude field is slightly larger than that of the chaotic field, which originates from the amplitude fluctuation of the Markovian stochastic field.

The attosecond sum-frequency RASPB indicate that beat signal oscillates not only temporally but also spatially along the direction $\Delta\mathbf{k}$, which is almost perpendicular to the propagation direction of the beat signal. Three normalized three-dimensional interferograms of the signal intensity $I(\Delta,\tau)$ versus time delay τ and frequency detuning Δ, $I(\tau,r)$ versus time delay τ and transverse position r, and $I(\Delta,r)$ versus frequency detuning Δ and transverse position r, respectively, have a smaller constant background caused by the intensity fluctuation of the narrowband chaotic field. At zero relative time delay ($\tau=0$), the twin beams originating from the same source enjoy perfect overlap at the sample of their corresponding noise patterns. This gives maximum interferometric contrast. As $|\tau|$ is increased, the interferometric contrast diminishes on the time scale that reflects material memory, usually much longer than the correlation time of the noisy light. The pure autocorrelation decay terms of the Rayleigh-active mode, the molecular-reorientational grating, and the laser fields for the RASPB originated from the amplitude fluctuation of the Markovian stochastic fields.

It is important to note that these three types of Markovian stochastic fields can have the same spectral density and thus the same second-order coherence function. The fundamental differences in the statistics of these fields are manifest only in the higher-order coherence functions [19,27]. The term "higher-order" refers to all orders larger than the second. In this paper, different stochastic models of the laser field only

affect the fourth-order coherence functions in the frequency and time domains. Due to the interference of the $\cos[\Delta\mathbf{k}\cdot\mathbf{r}-(\omega_1+\omega_3)\tau]$ and $\sin[\Delta\mathbf{k}\cdot\mathbf{r}-(\omega_1+\omega_3)\tau]$ factors, the temporal behavior of the RASPB is asymmetric with the maximum of the beat signal shifted from $\tau=0$ [Fig. 9(a)], whereas in the limit of $\Delta\rightarrow\infty$, the term with the $\sin[\Delta\mathbf{k}\cdot\mathbf{r}-(\omega_1+\omega_3)\tau]$ factor will disappear, and then the beat signal exhibits a symmetric behavior. The peak-to-background contrast ratio of the chaotic field is larger than that of the Gaussian-amplitude field or the phase-diffusion field. Furthermore, the contrast ratio of the phase-diffusion field is slightly larger than that of the Gaussian-amplitude field. The physical explanation for this is that the signal contrast ratio is equally sensitive to the amplitude and phase fluctuations of the Markovian stochastic fields. The polarization beat signal is shown to be particularly sensitive to the statistical properties of the Markovian stochastic light fields with arbitrary bandwidth. The Δ- or τ-independent constant background of the beat signal for a Gaussian-amplitude field or a chaotic field is much larger than that of the signal for a phase-diffusion field in Fig. 9. The physical explanation for this is that the Gaussian-amplitude field undergoes stronger intensity fluctuations than a chaotic field. On the other hand, the intensity (amplitude) fluctuations of the Gaussian-amplitude field or the chaotic field are always much larger than the pure phase fluctuations of the phase-diffusion field.

Next, we discuss the chromophore $P^{(3)}$ difference between the sum-frequency RASPB with a phase-conjugation geometry and the sum-frequency UMS [1] with a self-diffraction geometry from a physical viewpoint. The frequencies and wave vectors of the sum-frequency UMS signal are $\omega_{s_1}=2\omega_1-\omega_1$, $\omega_{s_2}=2\omega_2-\omega_2$ and $\mathbf{k}_{s_1}=2\mathbf{k}_1-\mathbf{k}_1'$, $\mathbf{k}_{s_2}=2\mathbf{k}_2'-\mathbf{k}_2$, respectively, which means that a photon is absorbed from each of the two mutually correlated fluctuating pump beams. On the other hand, the frequencies and wave vectors of the sum-frequency RASPB signal are $\omega_{s_1}=\omega_1-\omega_1+\omega_3$, $\omega_{s_2}=\omega_3-\omega_3+\omega_3$ and $\mathbf{k}_{s_1}=\mathbf{k}_1-\mathbf{k}_1'+\mathbf{k}_3$, $\mathbf{k}_{s_2}=\mathbf{k}_2'-\mathbf{k}_2+\mathbf{k}_3$, respectively [Fig. 1(c)]; therefore photons are absorbed from and emitted to the mutually correlated fluctuating twin beams 1 and 2, respectively. This difference between RASPB and UMS has a profound influence on the field-correlation effects. We note that the roles of beams 1 and 2 are interchangeable in the UMS, this interchangeable feature also makes the second-order coherence function theory failure in the UMS. Due to $\langle u(t_1)u(t_2)\rangle=0$, the absolute square of the stochastic average of the polarization $|\langle P^{(3)}\rangle|^2$ cannot be used to describe the temporal behavior of the sum-frequency UMS [1]. Our higher-order correlation (intensity correlation) treatment also is of vital importance in the sum-frequency UMS. Moreover, because $\langle u_i(t)\rangle=0$ and $\langle u_i^*(t)\rangle=0$, the absolute square of the stochastic average of the polarization $|\langle P^{(3)}\rangle|^2$, which involves second-order coherence function of $u_i(t)$, cannot be used to describe the temporal behavior of the RASPB. The sixth-order correlation theory $\langle|P^{(3)}|^2\rangle$ reduces to the second-order correlation theory $|\langle P^{(3)}\rangle|^2$ in the case that the laser pulse width is much longer than the laser coherence time. The second-order coherence function theory is valid when we are only interested in the τ-dependent part of the beating signal [21]. Therefore, the fourth-order coherence function theory is of vital importance in sum-frequency RASPB. The application of higher-order results to the difference-frequency RASPB experiment yielded a better fit to the data than an expression involving only second-order coherence [20–26]. Apparently the nature of the Markovian field has a more drastic effect on the outcome of the experiment than the underlying molecular nonlinearity. Since real laser fields are unlikely to behave like the pure three-field classes, a complicated superposition of various types of responses is to be expected.

V. HETERODYNE DETECTION OF SUM-FREQUENCY RASPB

The phase-sensitive detection of RFWM is based on the polarization interference between two FWM processes. Since optical fields oscillate too quickly for direct detection, they must be measured "in quadrature"—as photons. There are two ways to achieve quadrature. One is homodyne detection in which the new polarization is measured at its quadrature $(P_1+P_3)[(P_1)^*+(P_3)^*]$. These signals must be proportional to $|\chi^{(3)}|^2$. Thus, $I_{\text{homodyne}}\propto|\chi^{(3)}|^2$ and all phase information in $\chi^{(3)}$ is lost. The second way to achieve quadrature is to introduce another polarization P_2 (called a reference signal) designed in frequency and wave vector to conjugate (go into quadrature) in its complex representation with the new polarization of interest. Thus, in the heterodyne case, the signal photons are derived from $(P_1+P_2+P_3)[(P_1)^*+(P_2)^*+(P_3)^*]$ or $I_{\text{heterodyne}}\propto\chi^{(3)}$ (the signal is linear rather than quadratic). In heterodyne-detected (3+1)-wave mixing, phase information is retained and one can take a full measure of the complex susceptibility, including its phase. The phase of the complex induced polarization $P^{(3)}$ determines how its energy will partition between class I (the absorbed or emitted active spectroscopy) and class II (the passive spectroscopy with a new launched field) [8–16].

We demonstrated a phase-sensitive method for studying the RFWM. The reference signal is another FWM signal, which propagates along the same optical path as the RFWM signal. This method is used for studying the phase dispersion of the third-order susceptibility $\chi^{(3)}$ and for the optical heterodyne detection of the RFWM signal. Based on three types of models described above, the subtle Markovian field correlation effects will be investigated in heterodyne detection of attosecond sum-frequency RASPB. Compare with the above homodyne detection scheme of attosecond sum-frequency RASPB, the composite twin beams 1 and 2 for the heterodyne detection scheme of attosecond sum-frequency RASPB also originate from the same color-locking noisy lights.

Polarization beating is based on the interference at the detector between FWM signals, which originate from the macroscopic polarizations excited simultaneously in the sample. It is preferred that all the polarizations have the same frequency. The frequencies of P_1, P_2, and P_3 are ω_3, while P_{R2} and P_{R3} have frequencies $\omega_1-\omega_2+\omega_3$ and $\omega_2-\omega_1+\omega_3$, respectively [17,18]. Furthermore, due to the phase mismatching, the FWM signals from P_{R2} and P_{R3} are usually much smaller than that from P_1, P_2, and P_3. So we have the

total third-order polarization $P^{(3)}=P_1+P_2+P_3$. The third-order nonlinear polarizations P_1+P_3 and P_2 correspond to the RFWM process and NDFWM process which have wave vectors $\mathbf{k}_1-\mathbf{k}_1'+\mathbf{k}_3$ and $\mathbf{k}_2'-\mathbf{k}_2+\mathbf{k}_3$, respectively. The sum-frequency RASPB signal is proportional to the average of the absolute square of $P^{(3)}$ over the random variable of the stochastic process, so that the signal intensity $I(\Delta,\tau)\propto\langle|P^{(3)}|^2\rangle=\langle P^{(3)}(P^{(3)})^*\rangle=\langle(P_1+P_2+P_3)[(P_1)^*+(P_2)^*+(P_3)^*]\rangle$ contains $3\times3=9$ different terms in the fourth- and second-order coherence functions of $u_i(t)$ in phase-conjugation geometry, where $\langle P_1P_1^*\rangle$, $\langle P_2P_2^*\rangle$, $\langle P_3P_3^*\rangle$, $\langle P_1P_3^*\rangle$, and $\langle P_1^*P_3\rangle$ are included in the $u_1(t)$ or $u_2(t)$ fourth-order coherence functions; while $\langle P_1P_2^*\rangle$, $\langle P_1^*P_2\rangle$, $\langle P_2P_3^*\rangle$, and $\langle P_2^*P_3\rangle$ are included in the $u_i(t)$ second-order coherence functions. In general, the RASPB of heterodyne detection (at the intensity level) can be viewed as built of the sum of three contributions $[I(\Delta,\tau)\propto I_{P_2}+I_{P_1,P_3}+I_{P_2,P_1,P_3}$, where $I_{P_2}=\langle P_2P_2^*\rangle$, $I_{P_1,P_3}=\langle P_1P_1^*\rangle+\langle P_3P_3^*\rangle+\langle P_1P_3^*\rangle+\langle P_1^*P_3\rangle$, and $I_{P_2,P_1,P_3}=\langle P_1P_2^*\rangle+\langle P_1^*P_2\rangle+\langle P_2P_3^*\rangle+\langle P_2^*P_3\rangle]$: (i) the nonresonant autocorrelation term I_{P_2} of the ω_2 molecular-reorientational grating, which includes $u_2(t)$ fourth-order and $u_3(t)$ second-order Markovian stochastic correlation functions; (ii) the autocorrelation term I_{P_1,P_3} (i.e., RFWM) of the ω_1 nonresonant molecular-reorientational grating and $\Delta=\omega_3-\omega_1\approx0$ Rayleigh resonant vibrational mode, which includes $u_1(t)$ fourth-order and $u_3(t)$ second-order Markovian stochastic correlation functions; (iii) the cross-correlation term I_{P_2,P_1,P_3} between I_{P_2} and I_{P_1,P_3}, which includes $u_1(t)$, $u_2(t)$, and $u_3(t)$ second-order Markovian stochastic correlation functions. In heterodyne detection, we assume that $I_{P_2}\gg I_{P_1,P_3}$ at intensity level ($\eta\chi\gg|\chi^{(3)}|$ at field level), so the reference signal that originates from the ω_2 frequency component of twin beams 1 and 2 is much larger than the RFWM signal that originates from the ω_1 frequency component of twin beams 1 and 2.

A. Heterodyne detection of the chaotic field

Based on the chaotic field, we first have the sum-frequency RASPB signal in heterodyne detection, for (i) $\tau>0$,

$$I(\Delta,\tau)\propto\chi^2\left[\frac{\eta^2\gamma}{\gamma+2\alpha_2}+\eta^2\exp(-2\alpha_2|\tau|)+\eta\left(A+A^*+\frac{A\gamma}{\gamma_a-i\Delta}+\frac{A^*\gamma}{\gamma_a+i\Delta}\right)\exp[-(\alpha_1+\alpha_2)|\tau|]\right]$$
$$=I_{P_2}+\chi^2\eta\left(A+A^*+\frac{A\gamma}{\gamma_a-i\Delta}+\frac{A^*\gamma}{\gamma_a+i\Delta}\right)\times\exp[-(\alpha_1+\alpha_2)|\tau|],\tag{19}$$

and (ii) $\tau<0$,

$$I(\Delta,\tau)\propto I_{P_2}-2\gamma\alpha_1\chi^2\eta\left(\frac{A\exp[-(\gamma_a-i\Delta)|\tau|]}{(\gamma_b-i\Delta)(\gamma_a-i\Delta)}+\frac{A^*\exp[-(\gamma_a+i\Delta)|\tau|]}{(\gamma_b+i\Delta)(\gamma_a+i\Delta)}\right\}+\chi^2\eta\left(\frac{A^*\gamma}{\gamma_b+i\Delta}+\frac{A\gamma}{\gamma_b-i\Delta}+A+A^*\right)\exp[-(\alpha_1+\alpha_2)|\tau|].\tag{20}$$

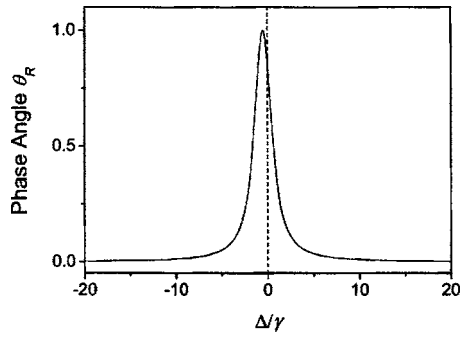

FIG. 10. Phase angle θ_R versus frequency detuning Δ/γ. Theoretical curve with $\alpha_1/\gamma=\alpha_2/\gamma=1$.

Here, $I_{P_2}=\chi^2[\eta^2\gamma/(\gamma+2\alpha_2)+\eta^2\exp(-2\alpha_2|\tau|)]$ for the chaotic field. The third-order susceptibility for RFWM consists of a Rayleigh-resonant term and a nonresonant term that originates from the ω_1 molecular-reorientational grating, i.e., $\chi^{(3)}=\chi+\chi\gamma/(\Delta-i\gamma')$, ($\gamma'=\gamma_a$ for $\tau>0$, whereas $\gamma'=\gamma_b$ for $\tau<0$). We express $\chi^{(3)}$ as $|\chi^{(3)}|\exp(i\theta_R)=|\chi^{(3)}|\cos\theta_R+i|\chi^{(3)}|\sin\theta_R$, with θ_R (Fig. 10) given by

$$\theta_R=\tan^{-1}\left(\frac{\gamma\gamma'}{(\gamma')^2+\Delta^2+\Delta\gamma'}\right)$$

We decompose the nonlinear susceptibility $\chi^{(3)}$ into a real and an imaginary part, i.e., $\chi^{(3)}=\chi'+i\chi''$, with $\chi'=\chi+\chi\gamma\Delta/[\Delta^2+(\gamma')^2]$, $\chi''=\chi\gamma'\gamma/[\Delta^2+(\gamma')^2]$.

Equations (19) and (20) indicate that the sum-frequency RASPB signal of heterodyne detection is modulated with a frequency $\omega_1+\omega_2$ as τ is varied. The phase of the signal oscillation depends on the phase θ_R of the nonlinear susceptibility. The two-color sum-frequency RASPB signal can also be employed for optical heterodyne detection to yield the real and the imaginary parts of the nonlinear susceptibility. From Eq. (19), we first have $I(\tau>0)\propto I_{P_2}+B+2|\chi^{(3)}|\chi\eta\exp[-(\alpha_1+\alpha_2)|\tau|]\sin(\theta_R-\theta)$; here $B=2\chi^2\eta(\cos\theta+\sin\theta)\exp[-(\alpha_1+\alpha_2)|\tau|]=B_0(\cos\theta+\sin\theta)$. If we adjust the time delay τ and $\mathbf{r}$ such that $\theta=\Delta\mathbf{k}\cdot\mathbf{r}-(\omega_1+\omega_2)\tau=2n\pi$, then $I(\tau>0)\propto(I_{P_2}+B_0)/\chi+2\eta\exp[-(\alpha_1+\alpha_2)|\tau|\chi''$. However, if $\theta=(2n+1/2)\pi$, we have $I(\tau>0)\propto(I_{P_2}+B_0)/\chi+2\eta\exp[-(\alpha_1+\alpha_2)|\tau|]\chi'$.

Secondly, we have from Eq. (20),

$$I(\tau<0)\propto I_{P_2}-2\gamma\alpha_1\chi^2\eta\exp(-\gamma_a|\tau|)\left(\frac{\exp[i(\theta+\Delta|\tau|)]}{(\gamma_b-i\Delta)(\gamma_a-i\Delta)}+\frac{\exp[-i(\theta+\Delta|\tau|)]}{(\gamma_b+i\Delta)(\gamma_a+i\Delta)}\right)+B+2|\chi^{(3)}|\chi\eta\exp[-(\alpha_1+\alpha_2)|\tau|]\sin(\theta_R-\theta).$$

If we adjust the time delay τ and $\mathbf{r}$ (if $\Delta|\tau|\approx0$) such that $\theta=2n\pi$, then

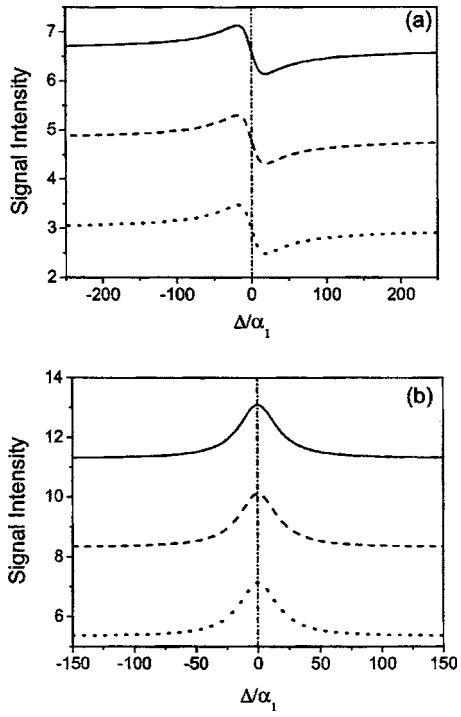

FIG. 11. The heterodyne detection spectra of the RASPB with (a) $\Delta\mathbf{k}\cdot\mathbf{r}-(\omega_1+\omega_2)\tau=0$, $\gamma\tau=0$ and (b) $\Delta\mathbf{k}\cdot\mathbf{r}-(\omega_1+\omega_2)\tau=\pi/2$, $\gamma\tau=5$. Theoretical curves represent the chaotic field (dashed line), phase-diffusion field (dotted line), and Gaussian-amplitude field (solid line) with parameters $\eta=0.3$, $\alpha_1/\gamma=\alpha_2/\gamma=0.06$, and $\alpha_3/\gamma=0.05$.

$$I(\tau<0)\propto(I_{P_2}+B_0)/\chi-\frac{4\gamma\alpha_1\chi\eta(\gamma_a\gamma_b-\Delta^2)}{(\gamma_a{}^2+\Delta^2)(\gamma_b{}^2+\Delta^2)}\exp(-\gamma_a|\tau|)+2\eta\exp[-(\alpha_1+\alpha_2)|\tau|\chi''.$$

However, if $\theta=(2n+1/2)\pi$, we have

$$I(\tau<0)\propto(I_{P_2}+B_0)/\chi+\frac{4\gamma\alpha_1\chi\eta\Delta(\gamma_a+\gamma_b)}{(\gamma_a{}^2+\Delta^2)(\gamma_b{}^2+\Delta^2)}\exp(-\gamma_a|\tau|)+2\eta\exp[-(\alpha_1+\alpha_2)|\tau|]\chi'.$$

In summary, by changing the time delay τ between twin beams 1 and 2 (if $\mathbf{r}=\mathbf{0}$) we can obtain the real [the dashed line of Fig. 11(a)] and imaginary [the dashed line of Fig. 11(b)] parts of $\chi^{(3)}$.

B. Heterodyne detection of the phase-diffusion field

Based on the phase-diffusion field, we then have the sum-frequency RASPB signal in heterodyne detection, for (i) $\tau>0$,

$$I(\Delta,\tau)\propto\chi^2\left[\frac{\gamma\eta^2}{\gamma+2\alpha_2}+\frac{2\alpha_2\eta^2\exp[-(\gamma+2\alpha_2)|\tau|]}{\gamma+2\alpha_2}+\eta\left(A+A^*+\frac{A\gamma}{\gamma_a-i\Delta}+\frac{A^*\gamma}{\gamma_a+i\Delta}\right)\exp[-(\alpha_1+\alpha_2)|\tau|]\right]$$
$$=I_{P_2}+\chi^2\eta\left(A+A^*+\frac{A\gamma}{\gamma_a-i\Delta}+\frac{A^*\gamma}{\gamma_a+i\Delta}\right)\times\exp[-(\alpha_1+\alpha_2)|\tau|],\quad(21)$$

and (ii) $\tau<0$,

$$I(\Delta,\tau)\propto I_{P_2}-2\gamma\alpha_1\chi^2\eta\left[\frac{A\exp[-(\gamma_a-i\Delta)|\tau|]}{(\gamma_a-i\Delta)(\gamma_b-i\Delta)}+\frac{A^*\exp[-(\gamma_a+i\Delta)|\tau|]}{(\gamma_a+i\Delta)(\gamma_b+i\Delta)}\right\}+\chi^2\eta\left(\frac{A^*\gamma}{\gamma_b+i\Delta}+\frac{A\gamma}{\gamma_b-i\Delta}+A+A^*\right)\exp[-(\alpha_1+\alpha_2)|\tau|]\Bigg].\quad(22)$$

Here,

$$I_{P_2}=\chi^2\eta^2\left(\frac{\gamma}{\gamma+2\alpha_2}+\frac{2\alpha_2\exp[-(\gamma+2\alpha_2)|\tau|]}{\gamma+2\alpha_2}\right)$$

for the phase-diffusion field. The high-order decay terms are reasonably neglected in the $\tau<0$ case. If $I_{P_2}\gg I_{P_1,P_3}$, we have $I(\tau>0)\propto I_{P_2}+B+2|\chi^{(3)}|\chi\eta\exp[-(\alpha_1+\alpha_2)|\tau|]\sin(\theta_R-\theta)$ from Eq. (21), and

$$I(\tau<0)\propto I_{P_2}-2\gamma\alpha_1\chi^2\eta\exp(-\gamma_a|\tau|)\left(\frac{\exp[i(\theta+\Delta|\tau|)]}{(\gamma_b-i\Delta)(\gamma_a-i\Delta)}+\frac{\exp[-i(\theta+\Delta|\tau|)]}{(\gamma_b+i\Delta)(\gamma_a+i\Delta)}\right)+B+2|\chi^{(3)}|\chi\eta\times\exp[-(\alpha_1+\alpha_2)|\tau|]\sin(\theta_R-\theta)$$

from Eq. (22), respectively. Except for the reference signal I_{P_2}, the heterodyne detection signal is the same as that of the heterodyne-detected chaotic-field case. By changing the time delay τ between twin beams 1 and 2 (if $\mathbf{r}=\mathbf{0}$) we can obtain the real [the dotted line of Fig. 11(a)] and imaginary [the dotted line of Fig. 11(b)] parts of $\chi^{(3)}$ for the phase-diffusion field. Due to the absence of the amplitude fluctuation, the solid curves of Fig. 11 have the smallest Δ-independent constant background.

C. Heterodyne detection of the real Gaussian field

Based on the real Gaussian field, we finally have the sum-frequency RASPB signal in heterodyne detection, for (i) $\tau>0$,

$$I(\Delta,\tau)\propto\chi^2\left[\frac{\eta^2\gamma}{\gamma+2\alpha_2}+\left(\frac{\eta^2\gamma}{\gamma+2\alpha_2}-\eta^2\right)\exp[-(\gamma+2\alpha_2)|\tau|]+2\eta^2\exp(-2\alpha_2|\tau|)+\eta\left(A+A^*+\frac{A\gamma}{\gamma_a-i\Delta}+\frac{A^*\gamma}{\gamma_a+i\Delta}\right)\exp[-(\alpha_1+\alpha_2)|\tau|]\right]$$
$$=I_{P_2}+\chi^2\eta\left(A+A^*+\frac{A\gamma}{\gamma_a-i\Delta}+\frac{A^*\gamma}{\gamma_a+i\Delta}\right)\times\exp[-(\alpha_1+\alpha_2)|\tau|],\quad(23)$$

and for (ii) $\tau<0$,

$$I(\Delta,\tau) \propto I_{P_2} - 2\gamma\alpha_1\chi^2\eta\left(\frac{A\exp[-(\gamma_a - i\Delta)|\tau|]}{(\gamma_b - i\Delta)(\gamma_a - i\Delta)} + \frac{A^*\exp[-(\gamma_a + i\Delta)|\tau|]}{(\gamma_b + i\Delta)(\gamma_a + i\Delta)}\right) + \chi^2\eta\left(\frac{A^*\gamma}{\gamma_b + i\Delta} + \frac{A\gamma}{\gamma_b - i\Delta} + A + A^*\right)\exp[-(\alpha_1 + \alpha_2)|\tau|]. \quad (24)$$

Here,

$$I_{P_2} = \chi^2\left[\frac{\eta^2\gamma}{\gamma + 2\alpha_2} + \left(\frac{\eta^2\gamma}{\gamma + 2\alpha_2} - \eta^2\right)\exp[-(\gamma + 2\alpha_2)|\tau|] + 2\eta^2\exp(-2\alpha_2|\tau|)\right]$$

for the real Gaussian field. The high-order decay terms are reasonably neglected in the $\tau < 0$ case. If the reference signal is much larger than the RFWM signal (i.e., $I_{P_2} \gg I_{P_1,P_3}$), except for I_{P_2} the heterodyne detection signal is also the same as that of the heterodyne-detected chaotic-field case. By changing the time delay τ between twin beams 1 and 2 (if $\mathbf{r}=\mathbf{0}$) we can obtain the real [the solid line of Fig. 11(a)] and imaginary [the solid line of Fig. 11(b)] parts of $\chi^{(3)}$ for the Gaussian-amplitude field. Due to the larger amplitude fluctuation, the dotted curves of Fig. 11 have the largest Δ-independent constant background.

VI. DISCUSSION AND CONCLUSION

Resonance-enhanced FWM has been employed for various different purposes. For example, it has been used to study the vibrational dephasing in molecular materials both in the frequency-domain and in the time-domain. One of the CRS techniques, which may be superior to all other CRS techniques, is Raman-enhanced nondegenerate four-wave mixing [7,17,18]. The main advantage of this technique is that the phase-matching condition is not so stringent and can be achieved over a very wide frequency range from many hundreds to thousands of cm^{-1}. It also possesses the features of nonresonant background suppression, excellent spatial signal resolution, free choice of interaction volume, and simple optical alignment. Specifically, in Raman-enhanced FWM the Raman vibration is excited by the simultaneous presence of two incident beams whose frequency difference equals the Raman excitation frequency and the Raman-enhanced FWM signal is the result of this resonant excitation. In contrast, Rayleigh-type FWM is a nonresonant process with no energy transfer between the light and the medium when the frequency difference between two incident beams equals zero. The resonant structure in the Rayleigh-type FWM spectrum is the result of an induced moving grating. This difference is also reflected in their line shapes. Specifically, unlike the Raman-enhanced FWM spectrum, which is asymmetric due to the interference between the resonant signal and the nonresonant background, the line shape of the Rayleigh-type FWM is always symmetric.

Rayleigh-type FWM is proposed for studying ultrafast processes in matter. In contrast to the conventional time-domain technique, Rayleigh-type FWM is a frequency-domain technique, therefore the time resolution is independent of the incident laser pulse width. Rayleigh-type FWM can be employed for the measurement of ultrafast longitudinal relaxation time in the frequency domain [7]. Based on field-correlation effects, this technique can be applied even to an absorbing medium if a time-delayed method is used. Rayleigh-type FWM is a third-order nonlinear phenomenon which involves three incident beams [see Fig. 1(a)]. Beams 1 and 2 have the same frequency ω_1 and a small angle θ exists between them. Beam 3 with frequency ω_3 is propagating along the opposite direction to beam 1. The FWM signal (beam 4) was propagated along a direction almost opposite that of beam 2. There are two mechanisms involved. First, the nonlinear interaction of beams 1 and 2 with the medium gives rise to a static molecular reorientational grating. The FWM signal is the result of the diffraction of beam 3 by the grating. Second, beams 2 and 3 with different frequencies build up a moving grating. If the grating lifetime τ_g is larger than the time it needs to move over one spatial period (which is of order $1/|\omega_1 - \omega_3|$), then destructive interference occurs during engraving and erases the grating. In other words, the signal originates from the spectral region $|\omega_1 - \omega_3| < 1/\tau_g$.

In general ultrashort pulses of equivalent bandwidth are not immune to dispersive effects (even when balanced) because the transform-limited light pulse is in fact temporally broadened (it is chirped) and this has drastic effects on its time resolution (the autocorrelation). In this sense the RASPB with double-frequency color-locking noisy light has an advantage [20–26]. Based on three stochastic models, the subtle Markovian field-correlation effects have been investigated in the homodyne or heterodyne detected RASPB. The different roles of the amplitude fluctuations and the phase fluctuations can be understood in time and frequency domains. The physical explanation for this is that the Gaussian-amplitude field undergoes stronger intensity fluctuations than a chaotic field. On the other hand, the intensity (amplitude) fluctuations of the Gaussian-amplitude field or the chaotic field are always much larger than the pure phase fluctuations of the phase-diffusion field.

Based on the polarization interference between nonresonant NDFWM and Rayleigh resonant RFWM processes, we can employ the RASPB to obtain the real and the imaginary parts of the Rayleigh resonance (Fig. 11). In the heterodyne detection of RASPB, we purposely introduce the nonresonant NDFWM signal by adding another component of noisy light with frequency ω_2 to twin composite beams 1 and 2, which propagates along the same optical path as the RFWM signal. The relative phase between the reference signal and RFWM signal is determined by the time delay τ between twin composite beams 1 and 2. Compared with the optical heterodyne detection Rayleigh-induced Kerr-effect method, because the polarizations of the incident beams can be adjusted independently RASPB is more convenient for studying various components of the fourth-rank tensor of third-order susceptibility. The RASPB has also been employed for studying the phase dispersion of $\chi^{(3)}$. Although this method is similar to the method of Ma *et al.* [9], we show that for Rayleigh resonance one can obtain the phase dispersion of $\chi^{(3)}$ by simply measuring the phase change of the FWM sig-

nal modulation as ω_3 is varied (Fig. 11). Generally speaking, this method can be applied to study the phase dispersion of $\chi^{(3)}$ in the RASPB.

In conclusion, a time-delayed method is proposed to suppress the thermal effect, and ultrafast longitudinal relaxation time can be measured even in an absorbing medium. One interesting feature in field-correlation effects is that RFWM exhibits temporal asymmetry and spectral symmetry. We also note that no coherence spike of RFWM with color-locking noisy light exists at $\tau=0$. RFWM exhibits hybrid radiation-matter detuning terahertz damping oscillation with a frequency close to Δ. Based on three stochastic models, the subtle Markovian field-correlation effects have been investigated in the homodyne- or heterodyne-detected RASPB and the heterodyne-detected RASPB. The analytic closed forms of the fourth-order Markovian stochastic correlations are characterized for homodyne (quadratic) and heterodyne (linear) detection, respectively. The heterodyne-detected signal of RASPB potentially offers rich dynamic information about the homogeneous broadening material phase of the third-order nonlinear susceptibility.

ACKNOWLEDGMENTS

This work was supported by the Chinese National Natural Sciences Foundation (Grant No. 60308002), the Foundation for the Author of National Excellent Doctoral Dissertation of PR China (Grant No. 200339), and the Science and Technology Research Key Project of Chinese Education Ministry (Grant No. 105156).

[1] D. DeBeer, E. Usadi, and S. R. Hartmann, Phys. Rev. Lett. **60**, 1262 (1988).
[2] V. L. Bogdanov, A. B. Evdokimov, G. V. Lukomskil, and B. D. Falnberg, JETP Lett. **49**, 157 (1989).
[3] H. Ma, A. S. L. Gomes, and Cid B. de Araujo, Opt. Lett. **17**, 1052 (1992).
[4] M. Xiao, Y. Q. Li, S. Jin, and J. Gea-Banacloche, Phys. Rev. Lett. **74**, 666 (1995).
[5] M. Xiao, IEEE J. Sel. Top. Quantum Electron. **9**, 86 (2003).
[6] N. Morita and T. Yajima, Phys. Rev. A **30**, 2525 (1984).
[7] P. M. Fu, Q. Jiang, X. Mi, and Z. H. Yu, Phys. Rev. Lett. **88**, 113902 (2002).
[8] T. F. Schulz, P. P. Aung, L. R. Weisel, K. M. Cosert, M. W. Gealy, and D. J. Ulness (unpublished).
[9] D. J. Ulness, J. Phys. Chem. A **107**, 8111 (2003).
[10] J. C. Kirkwood and A. C. Albrecht, J. Raman Spectrosc. **31**, 107 (2000).
[11] J. C. Kirkwood, D. J. Ulness, and A. C. Albrecht, J. Phys. Chem. A **104**, 4167 (2000).
[12] M. A. Dugan and A. C. Albrecht, Phys. Rev. A **43**, 3877 (1991).
[13] D. C. DeMott, D. J. Ulness, and A. C. Albrecht, Phys. Rev. A **55**, 761 (1997).
[14] D. J. Ulness and A. C. Albrecht, J. Raman Spectrosc. **28**, 571 (1997).
[15] M. J. Stimson, D. J. Ulness, and A. C. Albrecht, J. Raman Spectrosc. **28**, 579 (1997).
[16] M. J. Stimson, D. J. Ulness, J. C. Kirkwood, and G. S. Boutis, J. Opt. Soc. Am. B **15**, 505 (1998).
[17] Y. P. Zhang, X. Hou, K. Q. Lu, and H. C. Wu, Opt. Commun. **184**, 265 (2000).
[18] Y. P. Zhang, C. L. Gan, K. Q. Lu, C. S. Li, and X. Hou, Opt. Commun. **205**, 163 (2002).
[19] Ce Chen, D. S. Elliott, M. W. Hamilton, C. Chen, D. S. Elliott, and M. W. Hamilton, Phys. Rev. Lett. **68**, 3531 (1992).
[20] Y. P. Zhang, C. L. Gan, J. P. Song, X. J. Yu, R. Q. Ma, H. Ge, C. S. Li, and K. Q. Lu, Phys. Rev. A **71**, 023802 (2005).
[21] P. M. Fu, X. Mi, Z. H. Yu, Q. Jiang, Y. P. Zhang, and X. F. Li, Phys. Rev. A **52**, 4867 (1995).
[22] Y. P. Zhang, L. Q. Sun, T. T. Tang, and P. M. Fu, Phys. Rev. A **61**, 053819 (2000).
[23] Y. P. Zhang, L. Q. Sun, T. T. Tang, and P. M. Fu, J. Opt. Soc. Am. B **17**, 690 (2000).
[24] Y. P. Zhang, T. T. Tang, L. Q. Sun, and P. M. Fu, Phys. Rev. A **61**, 023809 (2000).
[25] Y. P. Zhang, C. B. de Araujo, and E. E. Eyler, Phys. Rev. A **63**, 043802 (2001).
[26] Y. P. Zhang, C. L. Gan, S. M. Farooqi, K. Q. Lu, X. Hou, and T. T. Tang, J. Opt. Soc. Am. B **19**, 1204 (2002).
[27] R. Bratfalean and P. Ewart, Phys. Rev. A **56**, 2267 (1997).